NASA-CR-193627

REPORT TO THE

NATIONAL AERONAUTICS AND SPACE ADMINISTRATION

SEMIANNUAL STATUS REPORT #5

for

GRANT NAG 5-1490

INVESTIGATION OF PASSIVE ATMOSPHERIC SOUNDING USING MILLIMETER AND SUBMILLIMETER WAVELENGTH CHANNELS

A.J. Gasiewski (Principal Investigator)

L.K. Adelberg (Graduate Student)
D.B. Kunkee (Graduate Student)
D.M. Jackson (Graduate Student)

Covering the period from

January 1, 1993 to June 30, 1993

Submitted by:

Professor Albin J. Gasiewski
School of Electrical Engineering
Georgia Institute of Technology
Atlanta, Georgia, 30332-0250
(404) 894-2934

NASA Technical Officer:

Dr. Robert F. Adler
Laboratory for Atmospheres/Code 612
NASA Goddard Space Flight Center
Greenbelt, MD 20771
(301) 286-9086

TABLE OF CONTENTS

I. INTRODUCTION 1

II. SUMMARY OF ACTIVITIES 3

III. CONCLUSIONS AND PLANS FOR FUTURE WORK 9

IV. REFERENCES 13

V. TABLES AND FIGURES 15

VI. APPENDIX A 22

INTRODUCTION

Progress by investigators at the Georgia Institute of Technology in the development of techniques for passive microwave retrieval of water vapor, cloud and precipitation parameters using millimeter- and sub-millimeter wavelength channels is reviewed. Channels of particular interest are in the tropospheric transmission windows at 90, 166, 220, 340 and 410 GHz and centered around the water vapor lines at 183 and 325 GHz. Collectively, these channels have potential application in high-resolution mapping (e.g., from geosynchronous orbit), remote sensing of cloud and precipitation parameters, and retrieval of water vapor profiles.

During the period from January 1, 1993 through June 30, the Millimeter-wave Imaging Radiometer (MIR) completed data flights during a two-month long deployment in conjunction with TOGA/COARE. Coincident data was collected from several other ground-based, airborne, and satellite sensors, including the NASA/MSFC AMPR, MIT MIS, DMSP SSM/T-2 satellite, collocated radiosondes, ground- and aircraft-based radiometers and cloud lidars, airborne infrared imagers, solar flux probes and airborne cloud particle sampling probes.

Optimal calibration of the MIR using a Wiener filter to facilitate estimating the instrument's gain and offset is being implemented for MIR data calibration and archiving. Reduction of the clear-air flight data shows good general agreement between MIR brightnesses and computed brightnesses based on coincident radiosondes, although the discrepancies between these brightnesses indicate that the humidity probes on AIR and VIZ type radiosondes indicate too moist of a reading in dry regions of the atmosphere.

In order to resolve questions concerning the absolute calibration of both the MIR and similar microwave sounders, the investigation of the scattering and emission from microwave blackbody calibration loads has continued. A new analytical formulation of the coupled wave method for lossy period surfaces has been developed, and an extension of the method to two-dimensional periodic structures is being developed. A preliminary thermal analysis for the wedge-type load is being applied to determine the

temperature profiles within such loads.

Integration of three submillimeter-wave channels on the MIR at 325+/-1,3, and 8 GHz is proceeding, and should be completed in time to obtain data from ER-2 flights planned for September, 1993.

A study commenced under this grant is the investigation of the utility of the third Stokes parameter $T_U=\langle E_v E_h^* \rangle$ for passive remote sensing of both ocean wave direction and oriented ice particles in cirrus clouds. Data from a polarimetric 92-GHz fixed-beam slant-path radiometer flown on the NASA DC-8 during TOGA/COARE is currently being reduced. Preliminary results from constant bank-angle maneuvers show brightness perturbations that are correlated with the direction of the aircraft, suggesting that information regarding the anisotropy of the ocean surface can be measured using passive radiometers.

SUMMARY OF ACTIVITIES

Activities within the period from January 1, 1993 through June 30, 1993 by Georgia Tech researchers in millimeter and submillimeter wavelength tropospheric remote sensing have focused on the optimal calibration and archiving of the MIR aircraft data, clear-air MIR data analysis, operation of the MIR aboard the NASA ER-2 during the Tropical Ocean Global Atmosphere/Coupled Ocean-Atmosphere Response Experiment (TOGA/COARE), and preliminary data analysis from TOGA/COARE. The MIR instrument is a joint project between NASA/GSFC and Georgia Tech. In the current configuration, the MIR has channels at 89, 150, 183+/-1,3,7, and 220 GHz. Provisions for three additional channels at 325+/-1,3 and 8 GHz have been made, and a 325-GHz receiver is currently being built by the ZAX Millimeter Wave Corporation for use in the MIR. Past Georgia Tech contributions to the MIR and its related scientific uses have included basic system design studies, performance analyses, circuit and radiometric load design, in-flight software, operation during deployment, post-flight data display software, and radiative transfer studies of the effects of clouds, water vapor, and precipitation on MIR brightnesses [Gasiewski, 1992].

In addition to the MIR-related activities, a 92-GHz polarimetric radiometer was deployed on the NASA DC-8 during TOGA/COARE. The purpose of this instrument was to investigate the relation between polarized microwave brightness temperatures and both oriented atmospheric ice cloud particles and anisotropic ocean surface features.

1. MIR Data Analysis

All in-flight MIR software for unattended operation aboard the NASA ER-2 has been completed. Post-flight data analysis tools under development include a graphical display program for the PC which incorporates optimal calibration filtering. MIR calibration is accomplished using hot and cold blackbody load views (once per scan) along with appropriately weighted temperature values from eight resistive temperature sensors located on the loads. Previous radiometer calibration techniques have used a causal infinite impulse response (IIR) discrete filter to provide estimates of the

instrument gain and offset values from the noisy single-scan estimates.

Recently, software has been written to demonstrate the application of an optimal non-causal filter (the Wiener filter) to estimate MIR gains and offsets [Adelberg et al, 1993]. The filter coefficients are derived from estimates of the autocorrelation functions for the gain and offsets of the instrument. As illustrated using clear-air MIR data (Figure 1), along-track brightness variances are reduced by ~10-70% using the optimal filter. The reductions are caused by the removal of calibration noise, bringing the resulting variance closer to the theoretical minimum given by $T_{sys}/\sqrt{B\tau}$. The improvements obtained using the optimal filter are most significant in the noisier channels (e.g,. 150, 183, 220 GHz); however, even the 90 GHz channel, which is relatively stable and quiet, shows improvement.[1] The software also incorporates compensation to correct for aircraft roll.

MIR data is being analyzed from flights during three ER-2 field deployments, summarized in Table 1. Applicable data from other instruments, including the Massachusetts Institute of Technology's Millimeter-wave Temperature Sounder (MTS), the NASA/MSFC Advanced Microwave Precipitation Radiometer (AMPR), the NASA Airborne Ocean Color Imager (AOCI), the DMSP SSM/T-2 radiometric sounder, the NASA/GSFC Raman water vapor lidar, and collocated radiosondes is currently being compiled. Several interesting case studies have been identified, and are outlined as follows:

(1) Multispectral simulation of the "warm ring" observed at the eyewall of tropical cyclone Oliver during TOGA/COARE. The extent to which this ~40-km diameter brightness ring is attributable to ocean surface roughness or low-altitude rain is currently unknown. Resolution of this question is expected to provide insight into the ability of high-resolution radiometry to differentiate between surface rain and oceanic wind, and the ability of high-resolution microwave radiometers to monitor the small-scale dynamics of tropical storms. Data from the MTS and AMPR radiometers and the JPL ARMAR rain radar on the DC-8 is being sought for use in this study.

(2) Millimeter-wave radiative transfer simulation of brightnesses observed over clouds. Investigators at the Kavieng site during TOGA/COARE

---

[1] A publication documenting the optimal filtering technique is being prepared for submission to the IEEE Transactions on Geoscience and Remote Sensing.

operated several ground-based instruments for cloud and water vapor sensing, including ground-based water vapor and cloud radiometers, a cloud lidar, and a cloud ceilometer. Data from approximately 3-4 coincident overflights of these instruments is being obtained[2] for the purpose of conducting comparisons between predicted and MIR-observed brightnesses over clouds.

(3) Clear-air MIR brightness data from both airborne and ground-based observations is being compared with radiative transfer calculations based on nearly coincident radiosondes and Raman lidar data. The results of these comparisons (shown in Figure 2 and Table 2) show that the relative humidity errors present in some types of standard radiosondes produces brightness variations (for both satellite- and ground-based observation geometries) that are much larger than the attainable accuracy of radiometers. This suggests that relative humidity, when averaged over a altitude range comparable to the temperature weighting function width, can ultimately be observed more accurately using radiometers than radiosondes. Moreover, the comparisons show that the AIR radiosonde provide a consistently positive bias in relative humidity, as evidenced by the fact the 183+/-1 GHz channel exhibits a large negative discrepancy for the airborne case, but the 150 GHz channel exhibits a large positive discrepancy for the ground-based case.[3]

(4) An interesting case of abrupt upper atmosphere drying across a convective front has been identified during TOGA/COARE ER-2 flight 93-053. The frontal crossing was also observed by the ER-2 lidar, thus clear-air regions can be unambiguously identified, and cloud top levels estimated. The drying caused an increase in brightness of ~12-14^{o} K in the 183+/-1 GHz channel over a distance of ~5 km; thus this case is expected to be useful in studies of the effects of spatial resolution on water vapor retrieval.

---

[2] Collaborating on the Kavieng overflights is Dr. E. Westwater of the NOAA Wave Propagation Laboratory in Boulder, CO.

[3] The results of this investigation being documented for submission to the IEEE Transactions on Geoscience and Remote Sensing.

2. Calibration Load Analysis

A new formulation of the coupled wave method [Gaylord and Moharam, 1982] based upon multiport linear network theory has been developed, and reflectivity calculations for several wedge absorber geometries have been performed.[4]

In order to predict the amount of thermal emission from a calibration target, the temperature distribution over the structure needs to be known. This is particularly critical near the tips of the absorber, where much of the emission occurs and thermal gradients are large. To this end, a steady state thermal analysis of a wedge-type structure has been continued. The solution to the heat equation is performed using the coupled harmonic method. Preliminary results suggest that thermal gradients near the absorbing (and, hence, emitting) tips of the wedges are significant enough to warrant consideration in calibration load analysis.

3. 325-GHz Receiver for use on the MIR

The implementation of a 325-GHz receiver on the MIR remains a high Georgia Tech priority. To achieve an acceptable noise figure (10-12 dB DSB) a modified design employing a fundamental mixer with DC bias and a frequency-tripled 108-GHz Gunn oscillator is being tested (Figure 3). Fabrication is being carried out by the ZAX Millimeter Wave Corporation of San Dimas, CA. A previous design using a double-balanced subharmonic mixer was fabricated by ZAX for installation during TOGA/COARE, but did not perform to required specifications. As of this writing, the receiver is expected to be available for integration into the MIR near the end of August 1993, and operative on the ER-2 for data flights during September-October, 1993.

4. Polarimetric Microwave Radiometry

While the utility of vertically and horizontally polarized brightness temperatures for both surface and atmospheric remote sensing has long been

---

[4] A paper documenting the coupled wave analysis has been submitted for publication in the IEEE Transactions on Antennas and Propagation [Gasiewski and Jackson, 1993; Appendix A].

recognized, the potential use of the third Stokes parameter $T_U=\langle E_V E_h^* \rangle$ in Earth remote sensing has largely been overlooked. Recent laboratory measurements using a fresh-water wave tank [Kunkee and Gasiewski, 1993] illustrate a significant dependence of T_U on the propagation direction of the water wave at 92 GHz. Moreover, the angular dependence complements that exhibited by T_V and T_H, suggesting that passive remote sensing of water surface wave direction can be facilitated by polarimetric microwave radiometry. As suggested by the work of Wentz [1992], polarimetric radiometry could have potential application in measuring ocean surface winds. Other investigations by Dzura et al [1992] suggest that polarimetric radiometry will also be useful for observing nonlinear ocean wave interactions. In addition to striated water surfaces, it is hypothesized that polarimetric microwave signatures in T_V, T_h, and T_U will be produced by oriented ice particles, for example, in electrified cirrus anvils. Indeed, microwave depolarization signatures in space-to-ground communications links have been associated with lightning discharges [Cox and Arnold, 1979].

To develop a theoretical model for the polarimetric surface emission process, we have implemented a geometrical optics model for the upwelling Stokes' vector. The model incorporates double scattering for steep observation angles. Using this model we have corroborated the (T_V,T_h,T_U) experimental data for the case of a 65^O observation angle (Figures 4a and b). The encouraging results of the laboratory wave tank experiment prompted an investigation into the practical application of polarimetric radiometry. Necessary electronic and hardware modifications to operate the NASA/GSFC 92-GHz polarimetric radiometer on the NASA DC-8 aircraft during TOGA/COARE were performed. The radiometer, developed under a previous NASA grant (NAG 8-829), permits precise measurement of the first three Stokes' parameters. Accurate pre- and post flight calibration data was collected using the polarized calibration load described by Gasiewski and Kunkee [1993]. A total of twenty DC-8 flights were made during TOGA/COARE, including seven low-altitude (~2-4 km) constant bank-angle maneuvers designed to provide constant observation angle views of the ocean surface over a range of

azimuthal angles.[5]

Post-mission calibration of some of the 92-GHz polarimetric data is complete. A plot of the constant bank-angle data for flight 93-01-13 shows residual peak-to-peak brightness variations with azimuthal angle for T_V and T_H of amplitude 2.5-6 K (Figures 5a and b). The beam observation angle relative to nadir is 65^o. The solid and dashed curves indicate $\cos(2\phi)$ and $\sin(2\phi)$ variations, (respectively), where ϕ is the azimuthal angle of observation with respect to the apparent wave direction. This data, along with the laboratory wave tank measurements corroborate the hypothesis that anisotropic ocean surface features can be observed using microwave radiometers.

---

[5] This is believed to be the first fully polarimetric radiometer to be operated in Earth remote sensing experiments on a US research aircraft. A predecessor 37-GHz instrument was flown during experiments conducted by the Soviets during the late 1980's [Dzura etal, 1992].

CONCLUSIONS AND PLANS FOR FUTURE WORK

To date, Georgia Tech has provided assistance to NASA/GSFC in the mechanical and electrical design of the MIR, and has been primarily responsible for MIR flight and analysis software. In addition, the investigations conducted over the past six months (1) confirm the utility of Wiener filtering in radiometric calibration, (2) illustrate significant humidity biases associated with certain types of radiosondes, particularly the AIR sondes, (3) have provided several case studies using MIR during TOGA/COARE, and (4) suggest the utility of fully polarimetric microwave radiometry for identifying ocean surface anisotropies, with the potential application to improving measurements of ocean surface wind direction.

1. MIR Observations and Data Analysis

At this time, our primary interests are the integration of the 325-GHz receiver into the MIR, EHF and SMMW radiative transfer studies using MIR data, and the development of EHF and SMMW meteorological retrieval algorithms. The EHF case studies will rely mostly on MIR data observed during TOGA/COARE and previous MIR flights, although new data, particularly at 325 GHz, is critical for both EHF and SMMW analyses.[6] At least one Georgia Tech investigator will be present to assist in the MIR deployment at Wallops Island during the September 1993 flights.

The highest Georgia Tech priority is integrating the 325-GHz receiver into the MIR for data flights during this deployment. Collaboration with ZAX will be made as necessary to help insure that this receiver is finished and available for the September flights. Alternate designs for the 325-GHz receiver are currently being studied in the event that the ZAX design cannot provide acceptable noise figures for airborne radiometric studies.

All MIR data is currently stored in raw format on high-density 8-mm tapes. To facilitate meteorological data analysis and provide a practical means of disseminating MIR data to collaborating investigators, the display

---

[6] Due to delays in fabricating the 325-GHz receiver, no SMMW data is yet available. A request to extend this grant through 1994 has been submitted so that such data can be obtained and analyzed.

software is being modified for disk-based storage. This software, which will be available for use on PC's, will also incorporate a variety of simple user-interactive features for MIR data analysis. The MIR data is also being archived on 35-mm slides for graphical storage and dissemination.

Two of the MIR case studies identified from TOGA/COARE are particularly interesting for radiative transfer experiments, namely, the overflights of cyclone Oliver and the Kavieng ground observation site. To this end, it is planned to simulate ocean surface and atmospheric conditions within the eye of cyclone Oliver to determine the consistency of wideband radiative transfer models and the observed brightness data. The radiative transfer model will consider the effects of increasing humidity, precipitation, and ocean roughness near the eyewall to determine the relative contributions of these components to the warm ring. This experiment will require some data from the NASA/MSFC AMPR and JPL ARMAR, both of which are available and are being requested.

The Kavieng overflights will be used to provide data for simulating the effects of clouds on upwelling EHF brightness temperatures. Ground-based radiometer data will be used to determine total water vapor and cloud content, while ground-based lidar will be used to determine cloud bottom altitudes.[7] Radiosondes will be further used to constrain the vertical distribution of water vapor. Of interest is a comparison of computed and observed upwelling brightness temperature, and in particular, the impact that clouds have on these temperatures.

In addition to validating radiative transfer models for TOGA/COARE case studies, high-resolution retrievals of water vapor and cloud water content from EHF and SMMW observations will be investigated. One promising method is the non-linear statistical iterative method used by Kuo [1988]. An extension of this technique to include cloud water content, base altitude, cloud thickness and surface emissivity as variable parameters is currently being studied. Another promising method is based on a multidimensional nonlinear map implemented using an artificial neural net. Here, the use of

---

[7] Airborne lidar data from the ER-2 CLS is not available for the Kavieng overflights.

the backpropagation algorithm to train a net consisting of two-layers (of about 10 neurons each) on simulated radiometric data is currently being studied, and will be continued.

2. Radiometer Calibration

In order to better characterize the RF response and absolute accuracy of the MIR, we plan to conduct several tests on the MIR, including: (1) RF passband response measurements using a plasma discharge noise source and IF spectrum analyzer, (2) local oscillator interference and reflection measurements using a stepped reflecting plate, and (3) calibration-load foam reflection and transmission measurements. These simple measurements will provide answers to questions concerning the calibration of the MIR and the use of the 183 and 325-GHz data in radiative transfer intercomparisons.

Accurate absolute calibration of the MIR requires that the total reflectivity of the hot and cold loads be less than 1%, and known to better than 0.1%. Manufacturer's specifications typically provide only the specular component of the reflectivity, which is thought to be substantially less than the total reflectivity. In order to refine the MIR calibration, we plan to extend the study of the electromagnetic characteristics of wedge-type blackbody loads to the more desirable pyramidal loads.

Our approach is to develop numerical models for one- and two-dimensionally periodic lossy gratings using the coupled wave method. We currently have software based on the coupled wave method to predict the reflectivity of one-dimensionally periodic loads of arbitrary dielectric profile. Extension of the coupled wave model to two-dimensionally periodic surfaces appears feasible, and will be attempted. In addition to the electromagnetic analysis, work on the steady state thermal analysis for one- and two-dimensionally periodic calibration loads will be continued. Although, the radiometric calibration load reflectivity analysis is of importance in understanding precision radiometer calibration, it is of tertiary importance relative to the EHF and SMMW data collection and analysis.

3. Polarimetric Radiometry

Further investigation of polarimetric radiometry under this grant will consist of analysis of 92-GHz polarimetric data observed during both TOGA/COARE and the laboratory wave-tank and striated soil and sand experiments. The limitations of the geometrical optics model in explaining the wave tank and ocean surface data will be of greatest interest; the validity of this model at 92-GHz will provide insight into the applicability of geometrical optics-based models for higher microwave frequencies. Information on the polarizing properties of surfaces will be useful in remote sensing of ocean characteristics and vegetation as well as understanding the effects of surface emission on passive atmospheric sounding.

To reduce the complexity of calibrating a polarimetric radiometer, the design of a digital cross-correlator will be continued. The cross correlator will be a precursor to the one proposed to be used on the NASA/MSFC Advanced Microwave Precipitation Radiometer (AMPR) [Gasiewski and Kunkee, 1992b]. The bandwidth of the cross-correlator will be approximately 500 MHz, making the device useful for wideband radiometric channel studies.

REFERENCES

Adelberg, L.K., A.J. Gasiewski and D.M. Jackson, "Optimal Calibration of Radiometers using Discrete Wiener Filters", accepted for presentation at the 1993 International Geoscience and Remote Sensing Symposium, Tokyo, Japan, August 18-23, 1993.

Cox, D.C., and H.W. Arnold, "Observations of Rapid Changes in the Orientation and Degree of Alignment of Ice Particles Along an Earth-Space Radio Propagation Path", J. Geophys. Res., vol. 84, pp. 5003-5010, 1979.

Dzura, M.S., V.S. Etkin, A.S. Khrupin, M.N. Pospelov, M.D. Raev, "Radiometers-Polarimeters: Principles of Design and Applications for Sea Surface Microwave Emission Polarimetry", Proceedings of the 1992 IEEE International Geoscience and Remote Sensing Symposium (IGARSS), pp. 1432-1434, June, 1992.

Gasiewski, A.J., "Numerical Sensitivity Analysis of Passive EHF and SMMW Channels to Tropospheric Water Vapor, Clouds, and Precipitation", IEEE Trans. Geosci. Remote Sensing, Vol. 30, No. 5, pp. 859-870, September, 1992.

Gasiewski, A.J., and D.M. Jackson, "Electromagnetic Scattering from Lossy Periodic Surfaces: Application to Microwave Absorbers", submitted for publication in IEEE Transactions on Antennas and Propagation, March, 1993.

Gasiewski, A.J., and D.B. Kunkee, "Calibration and Applications of Polarization Correlation Radiometers", To appear in IEEE Trans. Microwave Theory Tech., May, 1993.

Kunkee, D.B., and A.J. Gasiewski, "Laboratory Measurements of Water Gravity Wave Characteristics using Full Polarization Microwave Radiometry", Proceedings of the 1993 URSI National Radio Science Meeting, p 155, presented at the University of Colorado, Boulder, CO, Jan 5-8, 1993.

Gasiewski, A.J., and D.B. Kunkee, "Airborne Full Polarization Radiometry Using the MSFC Advanced Microwave Precipitation Radiometer (AMPR)", NASA Marshall Space Flight Center Earth Science and Applications Programs 1992 Research Review, Huntsville, AL, July 7-9, 1992b.

Kuo, C.C., "Statistical Iterative Scheme for Estimating Relative Humidity Profiles from Microwave Radiometric Measurements", S.M. Thesis, Massachusetts Institute of Technology, Cambridge, MA, 1988.

Moharam, M.G., and T.K. Gaylord, "Diffraction Analysis of Dielectric Surface Relief Gratings", J. Opt. Soc. Am., 72, 10, 1385-1392, 1982.

Wentz, F.J., "Measurement of Oceanic Wind Vector Using Satellite Microwave Radiometers", IEEE Trans. Geosci. Remote Sensing, vol. 30, no. 5, pp. 960-972, September 1992.

Table 1.

MIR integration and data flights: 1992-93.

Sortie #	Date	Time (UTC)	Instruments & Remarks
92-087	5/11/92	1900-2200	MIR,MIS(u),AOCI
92-089	5/14/92	2315-0515	MIR,MIS(d),AOCI *
92-090	5/15/92	2320-0500	MIR,MIS(u),AOCI *
92-130	7/23/92	2100-2315	MIS(d)
92-131	7/29/92	0700-1330	MIS(d) +*
92-132	7/30/92	0700-1330	MIS(d) +*
92-134	8/2/92	0700-1030	MIS(d) +
92-135	8/3/92	0700-0615	MIS(u) +
92-140	8/6/92	0700-1330	MIS(u) +*
93-053	1/12/93	2130-0430	Radiation (93-01-06)
93-054	1/17/93	2300-0710	Convection (93-01-07)
93-055	1/19/93	0130-0922	Convection (93-01-08)
93-056	1/25/93	2315-0700	Radiation/Kavieng (93-01-09)
93-057	1/30/93		Pilot proficiency
93-058	1/31/93	2200-0600	Radiation (93-01-10)
93-060	2/5/93	1430-2050	Convection, Oliver overflight (93-01-11) *
93-061	2/7/93	1555-2115	Cyclone Oliver, MIS(d)
93-062	2/9/93	1815-0025	Oliver overflight (93-01-13)
93-063	2/10/93	1430-2225	Kavieng, MIS(d) (93-01-14) *
93-064	2/19/93		Pilot proficiency, MIS(u)
93-065	2/20/93	1900-0335	Convection (93-01-16)
93-066	2/22/93	1900-0205	Convection (93-01-17)
93-067	2/24/93	2000-0315	Radiation (93-01-08)

* SSM/T-2 satellite underpass.
+ Ground-based Raman H_2O_v lidar overflight.
(xx-xx-xx) indicate coincident DC-8 flights.

Note: "u" or "d" indicate up-looking or down-looking, respectively.

Radiosonde Instrument Type	Frequency (GHz)					
	89	150	183±1	183±3	183±7	220
AIR						
Mean (K)	3.73	2.78	-11.49	-6.92	-3.27	0.00
Std. Dev. (K)	2.82	3.45	3.61	3.49	2.27	1.36
# samples	18	18	18	18	18	18
VIZ						
Mean (K)	3.93	1.85	-6.93	-2.63	-0.67	-0.03
Std. Dev. (K)	2.84	1.02	1.59	1.57	0.94	0.61
# samples	9	9	9	9	9	9
Viasala						
Mean (K)	-1.98	-1.04	-2.70	-0.20	0.79	0.53
Std. Dev. (K)	2.07	1.80	3.06	1.88	1.34	0.76
# samples	12	12	12	12	12	12
Lidar (w/AIR)						
Mean (K)	0.22	0.94	-11.65	-5.05	-1.83	0.15
Std. Dev. (K)	2.30	3.16	3.20	2.47	1.89	1.94
# samples	125	125	125	125	125	125
Lidar (w/Vaisala)						
Mean (K)	0.15	0.52	-6.48	-2.94	-0.63	0.06
Std. Dev. (K)	1.80	1.83	2.16	1.43	1.08	0.86
# samples	69	69	69	69	69	69

Table 2. Comparison of nadiral airborne computed and observed brightness for MIR channels using AIR, VIZ and Vaisala-type radiosondes. The data are from the Wallops Islands aircraft flights (see Table 1).

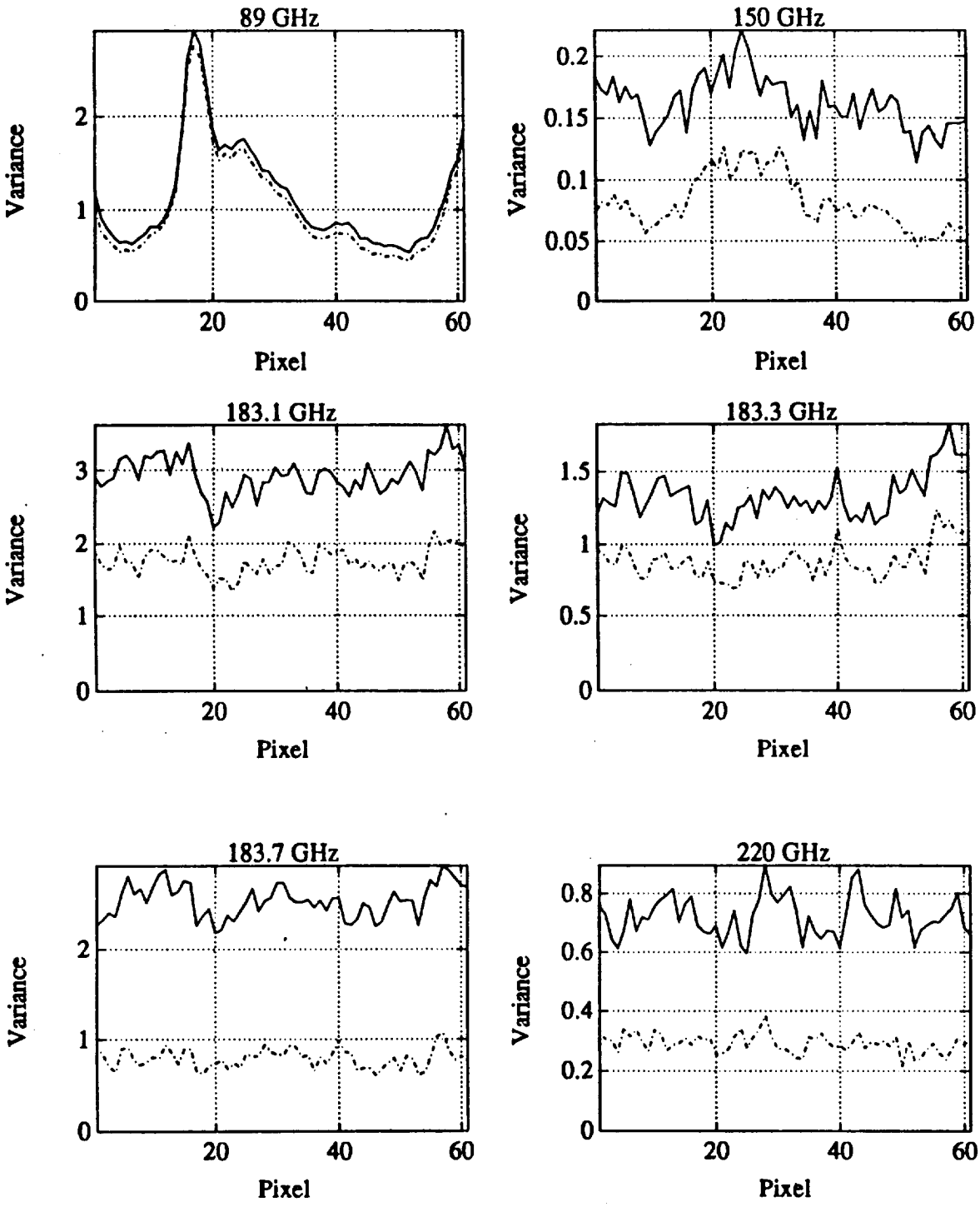

Figure 1: Brightness variance (in K^2) vs. scan angle (i.e., pixel number) for MIR data calibrated using an IIR filter (solid curves) and an optimal Wiener filter. Variance reductions of ~10-70% are obtained using the optimal filter.

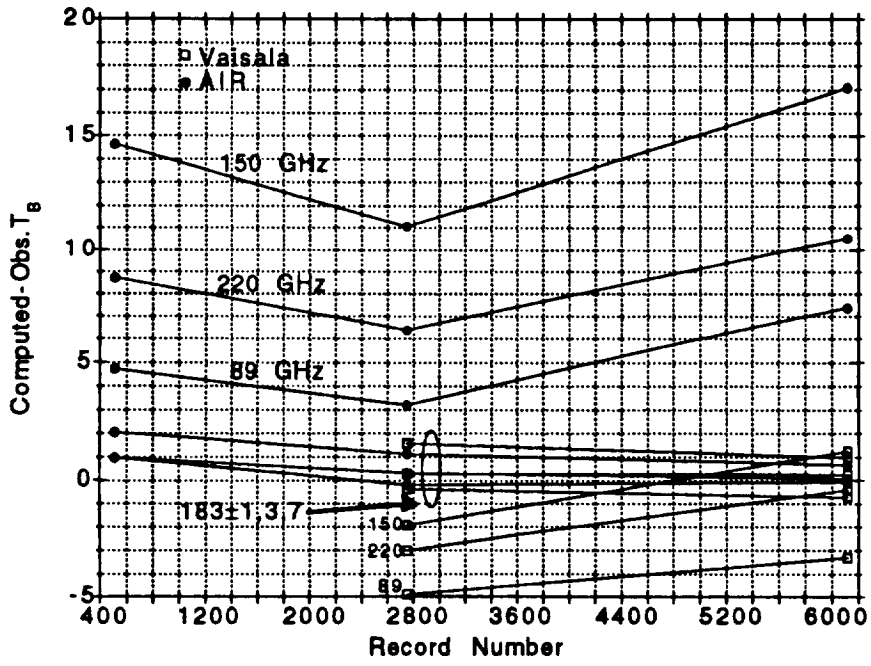

Figure 2. Comparison of ground-based computed and observed brightness for MIR channels using AIR and Vaisala-type radiosondes. The data is from Wallops Island on 7/30/92.

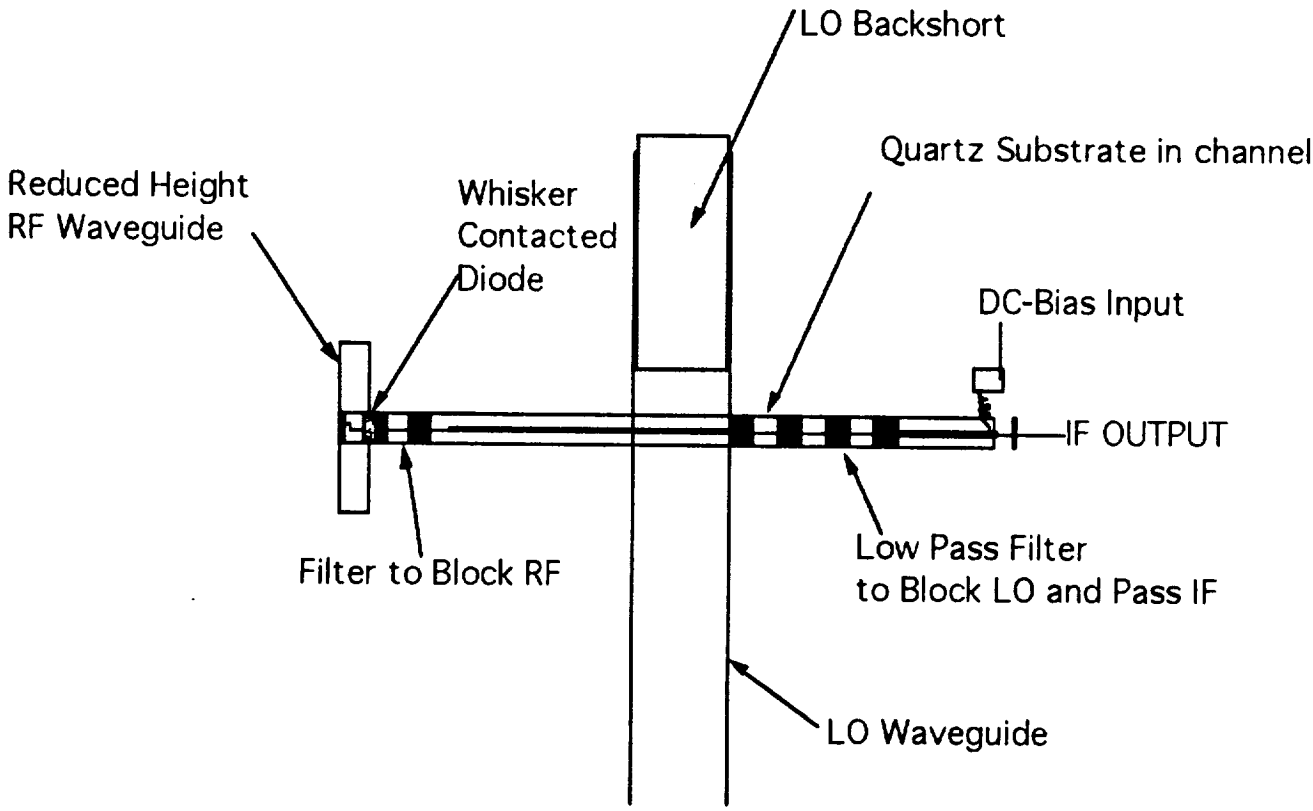

Figure 3. 325-Ghz mixer configuration, using waveguide Schottky diode mixing with a fundamental local oscillator.

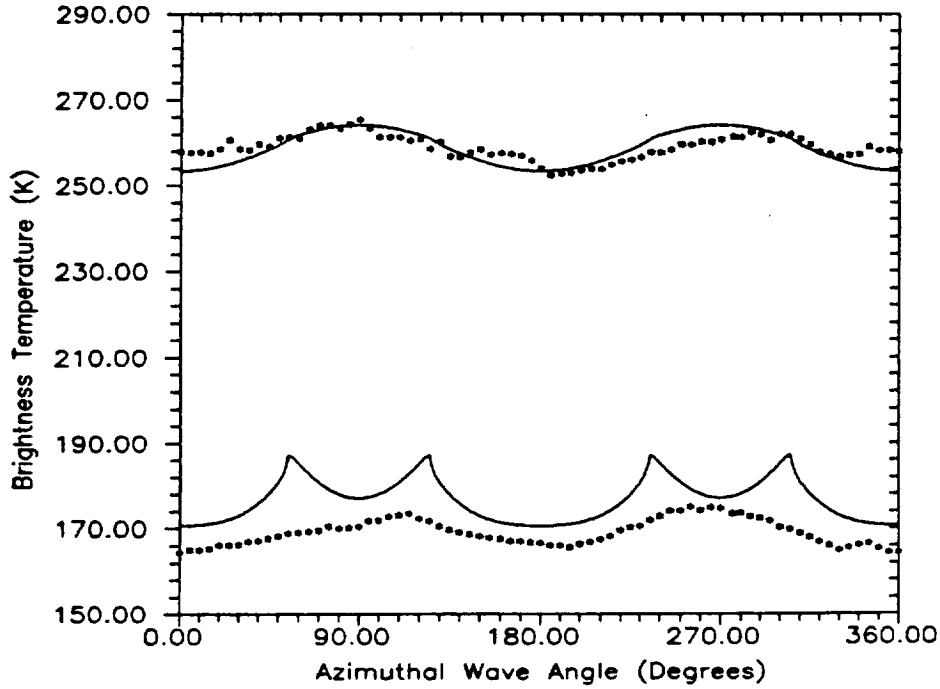

(a)

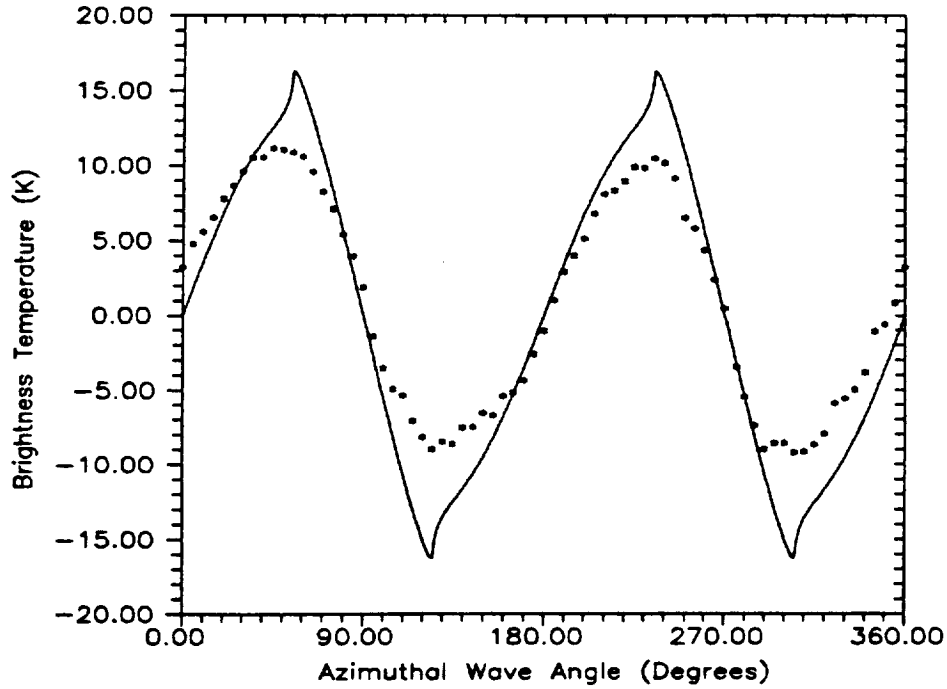

(b)

Figure 4. Polarimetric brightnesses compared to model calculations for laboratory wave tank measurements at 92 GHz: (a) T_v and T_h, (b) T_U. The observation angle is ~65° from nadir.

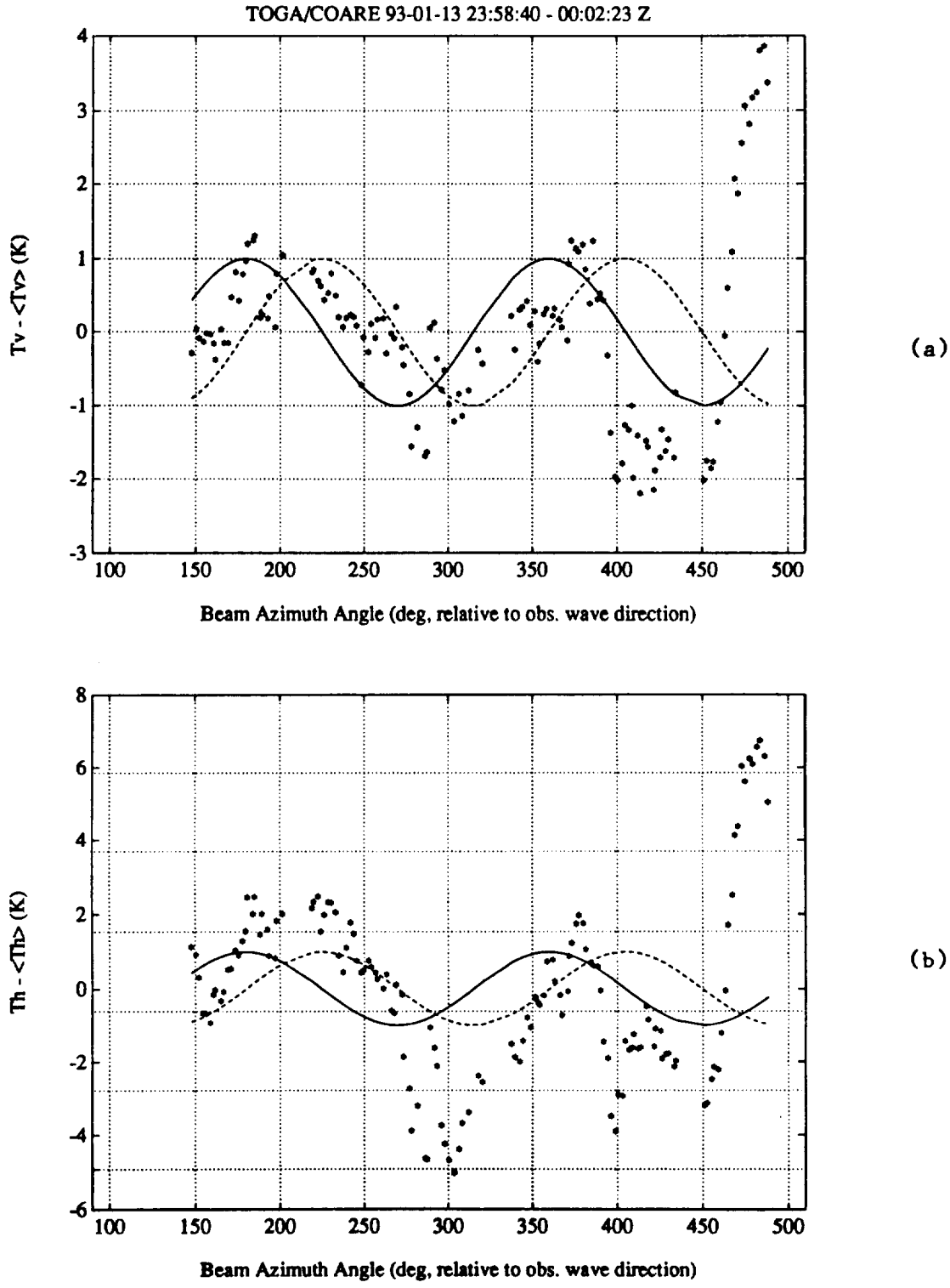

Figure 5. Vertical (a) and horizontal (b) 92-GHz brightness perturbations observed during constant bank-angle turns over ocean during TOGA/COARE. The beam angle is ~65° from nadir.

Appendix A.

Electromagnetic Scattering from Lossy Periodic Surfaces: Application to Microwave Absorbers

A.J. Gasiewski and D.M. Jackson

School of Electrical Engineering
Georgia Institute of Technology
Atlanta, Georgia 30332-0250

Submitted for publication in:

IEEE Transactions
on
Antennas and Propagation

March 5, 1993

Abstract

The scattered, transmitted and internal fields of a lossy periodic absorber illuminated by a plane wave are analyzed using coupled wave theory. The solution is facilitated by a cascaded linear-multiport formulation in which each layer of the periodic structure is considered to be a linear multiport network. A method for determining the required number of harmonics for acceptable convergence of the coupled-wave field expansions is developed.

The coupled wave reflectivity calculations are corroborated by measured data obtained from millimeter-wave bistatic scattering measurements of wedge-corrugated radiometer calibration targets. The angular response of the scattering range antennas is remove by deconvolution using the CLEAN algorithm. The coupled wave reflectivities are also shown to be consistent with calculations based on an integral equation method.

Using the coupled wave method, design data for wedge-corrugated iron-epoxy calibration targets is presented. The calculations show that total reflectivities of less than -30 dB over a decade in bandwidth are practical.

1 Introduction

In the design of blackbody targets for microwave radiometer calibration, the scattering and emission characteristics of periodic lossy dielectric structures are of great interest. For precise absolute calibration, it is required that the radiated brightness temperature of the surface be known to within ± 0.1 K or better. This, in turn, requires that the emitted radiation intensity be known to within ± 0.03 % or better. Given the uncertainty in the brightness of typical background radiation fields, this also requires that the total fraction of radiation reflected from the target, or total reflectivity, be extremely small (often less than -30 dB). Since the total reflectivity accounts for scattered radiation that can be incident from any angle, this quantity is larger than the commonly-measured retroreflectivity, or backscattering cross-section.

In determining both the emitted radiation intensity and the total reflectivity, it is essential to know the full solution for the electromagnetic fields scattered from, transmitted through, and internal to a periodic structure illuminated by an incident plane wave. From this solution, the emitted intensity can be obtained using detailed balancing, along with knowledge of the structure's temperature distribution. Likewise, the total reflectivity can be obtained from the full solution by computing the bistatic scattering coefficient of the structure. The full solution is also useful in the design of anechoic material for RF absorption and frequency selective surfaces used in antenna components, microwave filters, optical dielectric gratings and acoustics filters.

We restrict ourselves in this paper to rigorous numerical solutions to the scattering problem, that is, those involving no analytical approximations to Maxwell's equations and the electromagnetic boundary conditions. These solutions are exact in the limit of infinite computational precision, memory and time. In practice, error in a rigorous numerical solution occurs only as a result of finite arithmetic precision and limited array sizes. Thus the solution is applicable to surfaces of arbitrary electrical scale. Indeed, electrical sizes in between the regions of applicability of geo-

metrical scattering (at short wavelengths, [1]) and the extended boundary condition method (at long wavelengths, [2]) are of interest in calibration target design. For such intermediate-sized surfaces the Rayleigh criterion for smoothness [3, 4, 5] is not generally satisfied. As a consequence, the surface exhibits a complex spectrum of both upward and downward travelling waves within the troughs.

Several rigorous numerical methods for periodic structure analysis have been developed. These fall under the general headings of integral equation methods using periodic Green's functions [6, 7, 8], finite difference methods [9], finite element methods [10], coupled wave methods [11] and variations or combinations of these [12]. In previous studies of microwave absorbers [1, 13, 8], only the retroreflectivity of the periodic surface had been considered. In this study, we consider both the total reflectivity (as in [6]) and the internal and transmitted fields. Due to its applicability to to general periodic structures which might contain voids, dielectric layers, and other inhomogeneities, the coupled wave method is preferred.

Rigorous coupled wave solutions to the TE case have been formulated for corrugated periodic surfaces [14] and to the TM case for non-corrugated dielectric gratings [15]. However, both of these formulations have relied upon solutions to inhomogeneous second-order vector wave equations. A more direct solution, particularly for the general incidence case, has been based upon the first-order curl equations, (c.f., Eqs. 14 and 15), but formulated only for non-corrugated dielectric gratings [16, 17]. This paper considers both TE and TM formulations for corrugated periodic surfaces based on the curl equations [18]. The formulation is symmetric in $\overline{E}$ and $\overline{H}$, and its solution is based on a simple analogy with a cascade of linear multiport networks (e.g., [19, 20]). Using the cascaded network formulation and employing generalized scattering matrix theory the full field solution can be efficiently computed.

The coupled wave theory is applied to the analysis and design of wedge-corrugated microwave absorbers. This one-dimensionally periodic structure is commonly used in microwave radiometry as a calibration target. Both the internal fields

and total reflectivities are shown. The calculations are verified against millimeter-wave laboratory bistatic scattering measurements. Due to the relatively wide angular response of the scattering range antennas, deconvolution of the measured data using the CLEAN algorithm [21, 22] is performed. The coupled-wave reflectivities also compare favorably with calculations performed using an integral equation method based on a periodic Green's function. Since it is often desireable to use only a single wideband target to calibrate a set of channels spanning over a decade (or more) in bandwidth, computed data for the design of wideband corrugated absorber surfaces based on the coupled wave calculations is presented.

2 Periodic Surface Scattering

The periodic surface scattering geometry for an obliquely incident, arbitrarily polarized uniform plane wave is illustrated in Fig. 1. The incident wave is

$$\overline{E}_i = \overline{E}_o e^{-j\overline{k}_i \cdot \overline{r}} \tag{1}$$

where the wave vector $\overline{k}_i = k_x\hat{x} + k_y\hat{y} + k_z\hat{z}$. The surface grating vector is $\overline{K} = K\hat{x}$, where $K = 2\pi/\Lambda$ and Λ is the period of the surface. The two homogeneous half-spaces (regions 1 and 3) are characterized by complex relative material parameters ϵ_1, μ_1 and ϵ_3, μ_3, where $\epsilon = \epsilon' - j\epsilon''$ and $\mu = \mu' - j\mu''$. The periodic inhomogeneous region exists from $z = 0$ down to $z = -d$.

The time harmonic Maxwell's equations for source-free media are:

$$\begin{aligned} \nabla \times \overline{E} &= -j\omega\mu\overline{H} \qquad \nabla \times \overline{H} = j\omega\epsilon\overline{E} \\ \nabla \cdot \epsilon\overline{E} &= 0 \qquad \nabla \cdot \mu\overline{H} = 0 \end{aligned} \tag{2}$$

where both $\epsilon(x, z)$ and $\mu(x, z)$ are periodic functions of x. Since the exciting field is also periodic in x, we can use the Bloch-Floquet theorem [23] to express the field solutions in the form:

$$\overline{F}(x + \Lambda, y, z) = e^{-jk_x\Lambda}\,\overline{F}(x, y, z) \tag{3}$$

where $\overline{F} = \overline{E}$ or $\overline{H}$. A complete solution for the fields in regions 1 and 3 can be written as a series of Floquet harmonics:

$$\overline{E}_1(x,y,z) = \overline{E}_i + \sum_{n=-\infty}^{\infty} \overline{R}_n \, e^{-j(k_{xn}x + k_y y + k_{1zn}z)} \tag{4}$$

$$\overline{E}_3(x,y,z) = \sum_{n=-\infty}^{\infty} \overline{T}_n \, e^{-j(k_{xn}x + k_y y + k_{3zn}z)} \tag{5}$$

where $\overline{R}_n$, $\overline{T}_n$ are unknown amplitudes. Due to phase matching across region 2, identical space harmonics of x and y are used in both regions 1 and 3. The Floquet condition (Eq. 3) requires that

$$k_{xn} = k_x + nK. \tag{6}$$

Since the field solutions must satisfy Maxwell's equations, we also have

$$k_{qzn} = \sqrt{k_q^2 - (k_{xn}^2 + k_y^2)} \quad q = 1,3 \tag{7}$$

where $k_1 = (\omega/c)\sqrt{\epsilon_1 \mu_1}$ and $k_3 = (\omega/c)\sqrt{\epsilon_3 \mu_3}$. The associated magnetic fields can be obtained from Eqs. 4 and 5 using Ampere's law.

Each Floquet harmonic represents a plane wave mode, the summation of which form a complete expansion for the scattered and transmitted fields. Only a finite number of these are propagating uniform plane waves; a countably infinite number of them are nonuniform evanescent plane waves. For the general case in which the plane of incidence does not contain the grating vector (i.e., $\phi_i \neq 0, \pi$) the wave vectors for the scattered propagating plane waves lie along a cone. In region 1, the polar and azimuthal angles for the n^{th} propagating scattered wave are:

$$\theta_s = \tan^{-1}[(k_{xn}^2 + k_y^2)/k_{1zn}] \tag{8}$$

$$\phi_s = \tan^{-1}[k_y/k_{xn}] \tag{9}$$

If either region 1 or 3 is lossless, the associated value of k_{qzn} is either positive real ($k_{qzn} = k'_{qzn}$) for propagating waves or negative imaginary ($k_{qzn} = -jk''_{qzn}$) for evanescant waves. If either region 1 or 3 is lossy, the values of k_q and k_{qzn} are complex, but k_{xn} and k_y remain purely real.

For the special case when $\phi_s = 0$ or π, the implications of the Floquet condition and phase matching are illustrated in Fig. 2. Propagating harmonics in regions 1 and 3 have associated wave vectors whose tips lie on two circles with radii equal to either k_1 or k_3 (respectively). For the evanescent harmonics, the imaginary component of each k_{qxn} is given by one of two hyperbolic curves, defined by $k_{xn}^2 - k_{qxn}^2 = k_q^2$, $q = 1, 3$.

2.1 Coupled Wave Analysis

In the coupled wave analysis for periodic surfaces [16, 17], region 2 is discretized into L inhomogeneous layers of equal thickness Δz (Fig. 3). Within the l^{th} layer, the complex relative permittivity and permeability can be represented approximately by known Fourier series:

$$\epsilon(x, z_l - \Delta z \leq z \leq z_l) \equiv \epsilon_l(x) = \sum_{n=-\infty}^{\infty} a_{nl} e^{jKnx} \tag{10}$$

$$\mu(x, z_l - \Delta z \leq z \leq z_l) \equiv \mu_l(x) = \sum_{n=-\infty}^{\infty} b_{nl} e^{jKnx} \tag{11}$$

where z_l is the top of the l^{th} layer, $l = 1, 2, \ldots L$. The electric and magnetic fields within each layer can similarly be represented by expansions in space-harmonic fields:

$$\overline{E}_{2l}(x, y, z) = \sum_{n=-\infty}^{\infty} \{E_{xln}(z)\hat{x} + E_{yln}(z)\hat{y} + E_{zln}(z)\hat{z}\} e^{-j(k_{xn}x + k_y y)} \tag{12}$$

$$\overline{H}_{2l}(x, y, z) = \sum_{n=-\infty}^{\infty} \{H_{xln}(z)\hat{x} + H_{yln}(z)\hat{y} + H_{zln}(z)\hat{z}\} e^{-j(k_{xn}x + k_y y)} \tag{13}$$

where the $E_{xln}, E_{yln}, E_{zln}$ and $H_{xln}, H_{yln}, H_{zln}$ are the unknown amplitudes of the n^{th} space harmonic.

Substitution of Eqs. 10-13 into Faraday's and Ampere's laws yields a set of differential equations in which all space harmonics of the electric field are coupled with all those of the magnetic field by virtue of the periodicity of ϵ and μ:

$$\nabla \times \overline{E}_{2l} = -j\omega\mu_o\mu_l(x)\overline{H}_{2l} \tag{14}$$

$$\nabla \times \overline{H}_{2l} = j\omega\epsilon_o\epsilon_l(x)\overline{E}_{2l} \tag{15}$$

The above equations can be harmonically balanced [24] to yield an infinite set of first-order coupled differential equations for the space harmonic amplitudes (the coupled wave equations):

$$\frac{d}{dz}\begin{bmatrix} \overline{E}_{xl} \\ \overline{E}_{yl} \\ \overline{H}_{xl} \\ \overline{H}_{yl} \end{bmatrix} = \overline{\overline{A}} \begin{bmatrix} \overline{E}_{xl} \\ \overline{E}_{yl} \\ \overline{H}_{xl} \\ \overline{H}_{yl} \end{bmatrix} \tag{16}$$

where

$$\overline{\overline{A}} = \left[\begin{array}{c|c} 0 & \overline{\overline{A}}_{12} \\ \hline \overline{\overline{A}}_{21} & 0 \end{array}\right] \tag{17}$$

and $\overline{E}_{zl}, \overline{H}_{zl}$ are determined directly from $\overline{E}_{xl}, \overline{E}_{yl}$ and $\overline{H}_{xl}, \overline{H}_{yl}$, respectively. The submatrices $\overline{\overline{A}}_{12}$ and $\overline{\overline{A}}_{21}$ can be computed in terms of known parameters such as $\omega, K, \overline{k}_i, a_{nl}$, and b_{nl}.

For the general incidence-angle case ($\phi \neq 0, \pi$), all of vector components of the the space harmonic amplitudes are coupled through the matrix $\overline{\overline{A}}$. However, for the special case of $\phi = 0, \pi$, the space harmonics produced by TE-polarized ($\overline{E}_o = E_o\hat{y}$) incident waves are decoupled from those produced by TM-polarized ($\overline{H}_o = H_o\hat{y}$)incident waves. In this case, a complete solution can be found by consideration of the TE and TM polarizations separately.

Consider a TM-polarized incident field with $\overline{H}_i = H_o\hat{y}e^{-j(k_x x + k_z z)}$, for which only H_{yl}, E_{xl} and E_{zl} will be nonzero. Upon harmonic balancing Eqs. 14 and 15 become:

$$\frac{d}{dz}E_{xln}(z) = -jk_{xn}E_{zln}(z) - j\eta_o k_o \sum_{m=-\infty}^{\infty} H_{ylm}(z)\, b_{m-n,l} \tag{18}$$

$$\frac{d}{dz}H_{yln}(z) = -j\frac{k_o}{\eta_o}\sum_{m=-\infty}^{\infty} E_{xlm}(z)\, a_{m-n,l} \tag{19}$$

$$E_{zln}(z) = -\eta_o \sum_{m=-\infty}^{\infty} \frac{k_{xm}}{k_o} H_{ylm}(z)\tilde{a}_{m-n,l} \tag{20}$$

for $n = -\infty \ldots \infty$, where the $\tilde{a}_{nl}$ are the Fourier coefficients for $1/\epsilon_l(x)$, $k_o = \omega\sqrt{\mu_o\epsilon_o}$ and $\eta_o = \sqrt{\mu_o/\epsilon_o}$. Since the E_{zl} are linearly related to H_{yl}, only two state variable functions (E_x and H_y) are required to completely specify the fields, and the coupled

wave equations reduce to the following first-order constant-coefficient linear system:

$$\frac{d}{dz}\begin{bmatrix}\overline{E}_{xl}\\ \overline{H}_{yl}\end{bmatrix} = \left[\begin{array}{c|c} 0 & \overline{\overline{A}}_{12} \\ \hline \overline{\overline{A}}_{21} & 0 \end{array}\right]\begin{bmatrix}\overline{E}_{xl}\\ \overline{H}_{yl}\end{bmatrix} \tag{21}$$

where

$$\left\{\overline{\overline{A}}_{12}\right\}_{nm} = j\eta_o k_o\left(\frac{k_{xm}k_{xn}}{k_o^2}\,\tilde{a}_{n-m,l} - b_{n-m,l}\right) \tag{22}$$

$$\left\{\overline{\overline{A}}_{21}\right\}_{nm} = -j\,\frac{k_o}{\eta_o}\,a_{n-m,l} \tag{23}$$

In practice, the above system is truncated at the N^{th} harmonic. Thus, the submatrices $\overline{\overline{A}}_{12}$ and $\overline{\overline{A}}_{21}$ are each of size $(2N+1)\times(2N+1)$.

A solution to Eq. 21 can be obtained by eigenanalysis, in which the space-harmonic amplitudes are expressed as a linear combination of eigenfunctions:

$$\begin{bmatrix}\overline{E}_{xl}\\ \overline{H}_{yl}\end{bmatrix} = \overline{\overline{W}}\;\overline{\overline{e}}(z)\;\overline{C} \tag{24}$$

where

$$\overline{\overline{e}}(z) \equiv \begin{bmatrix} e^{\lambda_1 z} & 0 & \cdots & 0 \\ 0 & e^{\lambda_2 z} & & \vdots \\ \vdots & & \ddots & 0 \\ 0 & \cdots & 0 & e^{\lambda_{2(2N+1)} z} \end{bmatrix} \tag{25}$$

In the above, the λ's are the eigenvalues of $\overline{\overline{A}}$ for the l^{th} layer, the columns of $\overline{\overline{W}}$ are the associated eigenvectors, and $\overline{C}$ is a vector of $2(2N+1)$ coefficients, to be determined by boundary conditions on the tangential $\overline{E}$ and $\overline{H}$ fields at the top and bottom of each layer.

2.2 Linear Multiport Solution

In the transmission matrix solution, each layer of the periodic structure is treated as an isolated linear multiport network (Fig. 4), with the layer's transmission matrix determined using coupled wave analysis. The transmission matrix for the entire periodic surface is subsequently obtained by multiplying, in sequence, the individual transmission matrices to form a multilayer transmission matrix.

Consider the incoming and outgoing plane wave modes for a single grating layer where both evanescent and propagating modes are included. For the TM case, the electric fields are represented as:

$$\overline{E}_1^+(x,z) = \sum_{n=-\infty}^{\infty} E_{1n}^+ \left\{ \frac{k_{zn}}{k_o}\hat{x} + \frac{k_{xn}}{k_o}\hat{z} \right\} e^{-j(k_{xn}x - k_{zn}(z-\Delta z))} \tag{26}$$

$$\overline{E}_1^-(x,z) = \sum_{n=-\infty}^{\infty} E_{1n}^- \left\{ \frac{k_{zn}}{k_o}\hat{x} - \frac{k_{xn}}{k_o}\hat{z} \right\} e^{-j(k_{xn}x + k_{zn}(z-\Delta z))} \tag{27}$$

$$\overline{E}_3^+(x,z) = \sum_{n=-\infty}^{\infty} E_{3n}^+ \left\{ \frac{k_{zn}}{k_o}\hat{x} - \frac{k_{xn}}{k_o}\hat{z} \right\} e^{-j(k_{xn}x + k_{zn}z)} \tag{28}$$

$$\overline{E}_3^-(x,z) = \sum_{n=-\infty}^{\infty} E_{3n}^- \left\{ \frac{k_{zn}}{k_o}\hat{x} + \frac{k_{xn}}{k_o}\hat{z} \right\} e^{-j(k_{xn}x - k_{zn}z)} \tag{29}$$

where the superscripts refer to incoming (+) or outgoing (−) waves, and $k_{zn} = \sqrt{k_o^2 - k_{xn}^2}$. The associated magnetic fields are:

$$\overline{H}_1^+(x,z) = \sum_{n=-\infty}^{\infty} \frac{-E_{1n}^+}{\eta_o}\hat{y}\, e^{-j(k_{xn}x - k_{zn}(z-\Delta z))} \tag{30}$$

$$\overline{H}_1^-(x,z) = \sum_{n=-\infty}^{\infty} \frac{E_{1n}^-}{\eta_o}\hat{y}\, e^{-j(k_{xn}x + k_{zn}(z-\Delta z))} \tag{31}$$

$$\overline{H}_3^+(x,z) = \sum_{n=-\infty}^{\infty} \frac{E_{3n}^+}{\eta_o}\hat{y}\, e^{-j(k_{xn}x + k_{zn}z)} \tag{32}$$

$$\overline{H}_3^-(x,z) = \sum_{n=-\infty}^{\infty} \frac{-E_{3n}^-}{\eta_o}\hat{y}\, e^{-j(k_{xn}x - k_{zn}z)} \tag{33}$$

The transmission matrix $\overline{\overline{T}}_l$ for the l^{th} layer is defined as:

$$\begin{bmatrix} \overline{E}_1^+ \\ \overline{E}_1^- \end{bmatrix} = \overline{\overline{T}}_l \begin{bmatrix} \overline{E}_3^- \\ \overline{E}_3^+ \end{bmatrix} = \left[\begin{array}{c|c} \overline{\overline{T}}_{11} & \overline{\overline{T}}_{13} \\ \hline \overline{\overline{T}}_{31} & \overline{\overline{T}}_{33} \end{array}\right] \begin{bmatrix} \overline{E}_3^- \\ \overline{E}_3^+ \end{bmatrix} \tag{34}$$

where $\overline{E}_1^+$, $\overline{E}_1^-$, $\overline{E}_3^+$, and $\overline{E}_3^-$ are vectors containing the plane wave amplitude coefficients. The four sub-matrices of $\overline{\overline{T}}_l$ are generalized transmission (matrix) coefficients [19]. They play the same role as the familiar scalar transmission coefficients in cascaded microwave circuit analysis.

By harmonic balancing, the tangential electric and magnetic field boundary conditions for the top ($z = \Delta z$) and bottom ($z = 0$) of the grating can be expressed

in matrix form as:

$$\left[\frac{\overline{\overline{Z}}_{TMo}(\overline{E}_1^+ + \overline{E}_1^-)}{(-\overline{E}_1^+ + \overline{E}_1^-)}\right] = \eta_o \overline{\overline{W}}\,\overline{\overline{e}}(\Delta z)\,\overline{C} \tag{35}$$

$$\left[\frac{\overline{\overline{Z}}_{TMo}(\overline{E}_3^+ + \overline{E}_3^-)}{(\overline{E}_3^+ - \overline{E}_3^-)}\right] = \eta_o \overline{\overline{W}}\,\overline{C} \tag{36}$$

where $\overline{\overline{Z}}_{TMo}$ is the TM wave impedance matrix for free space, with diagonal elements $k_{ozn}\eta_o/k_o$ and zeros elsewhere. The generalized transmission matrix coefficients are subsequently determined by solving Eqs. 35 and 36 under the conditions that $\overline{E}_3^+ = 0$ (for $\overline{\overline{T}}_{11}$ and $\overline{\overline{T}}_{31}$), and, alternately, $\overline{E}_3^- = 0$ (for $\overline{\overline{T}}_{13}$ and $\overline{\overline{T}}_{33}$). These steps lead to:

$$\begin{aligned}
\overline{\overline{T}}_{11} &= \frac{1}{2}\left[\overline{\overline{Z}}_{TMo}^{-1}(\overline{\overline{P}}_{EE}(\Delta z)\overline{\overline{Z}}_{TMo} - \overline{\overline{P}}_{EH}(\Delta z)) - \overline{\overline{P}}_{HE}(\Delta z)\overline{\overline{Z}}_{TMo} + \overline{\overline{P}}_{HH}(\Delta z)\right] \\
\overline{\overline{T}}_{31} &= \frac{1}{2}\left[\overline{\overline{Z}}_{TMo}^{-1}(\overline{\overline{P}}_{EE}(\Delta z)\overline{\overline{Z}}_{TMo} - \overline{\overline{P}}_{EH}(\Delta z)) + \overline{\overline{P}}_{HE}(\Delta z)\overline{\overline{Z}}_{TMo} - \overline{\overline{P}}_{HH}(\Delta z)\right] \\
\overline{\overline{T}}_{13} &= \frac{1}{2}\left[\overline{\overline{Z}}_{TMo}^{-1}(\overline{\overline{P}}_{EE}(\Delta z)\overline{\overline{Z}}_{TMo} + \overline{\overline{P}}_{EH}(\Delta z)) - \overline{\overline{P}}_{HE}(\Delta z)\overline{\overline{Z}}_{TMo} - \overline{\overline{P}}_{HH}(\Delta z)\right] \\
\overline{\overline{T}}_{33} &= \frac{1}{2}\left[\overline{\overline{Z}}_{TMo}^{-1}(\overline{\overline{P}}_{EE}(\Delta z)\overline{\overline{Z}}_{TMo} + \overline{\overline{P}}_{EH}(\Delta z)) + \overline{\overline{P}}_{HE}(\Delta z)\overline{\overline{Z}}_{TMo} + \overline{\overline{P}}_{HH}(\Delta z)\right]
\end{aligned} \tag{37}$$

where the $\overline{\overline{P}}_{ij}$ are the four sub-matrices of the propagator matrix $\overline{\overline{P}}(\Delta z)$ (e.g., see [25]):

$$\overline{\overline{P}}(\Delta z) = \left[\begin{array}{c|c} \overline{\overline{P}}_{EE}(\Delta z) & \overline{\overline{P}}_{EH}(\Delta z) \\ \hline \overline{\overline{P}}_{HE}(\Delta z) & \overline{\overline{P}}_{HH}(\Delta z) \end{array}\right] = \overline{\overline{W}}\,\overline{\overline{e}}(\Delta z)\,\overline{\overline{W}}^{-1} \tag{38}$$

To find the overall transmission matrix for a multilayer structure, the transmission matrices for the individual layers are cascaded [19, 20]:

$$\overline{\overline{T}} = \overline{\overline{T}}_1\overline{\overline{T}}_2\overline{\overline{T}}_3 \ldots \overline{\overline{T}}_{L-1}\overline{\overline{T}}_L \tag{39}$$

Note that $\overline{\overline{T}}$ is computed under the assumption of η_o as the normalizing characteristic impedance. To determine the transmission matrix for arbitrary bounding media, we must re-normalize to the impedances of the upper and lower half spaces. This is accomplished by first computing the impedance matrix $\overline{\overline{Z}}$ of the structure, defined implicitly by:

$$\left[\frac{\overline{\overline{Z}}_{TMo}/\eta_o(\overline{E}_1^+ + \overline{E}_1^-)}{\overline{\overline{Z}}_{TMo}/\eta_o(\overline{E}_3^+ + \overline{E}_3^-)}\right] = \overline{\overline{Z}}\left[\frac{(-\overline{E}_1^+ + \overline{E}_1^-)/\eta_o}{(\overline{E}_3^+ - \overline{E}_3^-)/\eta_o}\right] \tag{40}$$

In terms of $\overline{\overline{T}}$:

$$\overline{\overline{Z}} = \left[\begin{array}{c|c} \overline{\overline{Z}}_{TMo} & \overline{\overline{0}} \\ \hline \overline{\overline{0}} & \overline{\overline{Z}}_{TMo} \end{array}\right] \left[\begin{array}{c|c} \overline{\overline{T}}_{33}+\overline{\overline{T}}_{13} & \overline{\overline{T}}_{31}+\overline{\overline{T}}_{11} \\ \hline \overline{\overline{I}} & \overline{\overline{I}} \end{array}\right] \left[\begin{array}{c|c} \overline{\overline{T}}_{33}-\overline{\overline{T}}_{13} & \overline{\overline{T}}_{31}-\overline{\overline{T}}_{11} \\ \hline \overline{\overline{I}} & -\overline{\overline{I}} \end{array}\right]^{-1}$$

$$= \left[\begin{array}{c|c} \overline{\overline{Z}}_{11} & \overline{\overline{Z}}_{13} \\ \hline \overline{\overline{Z}}_{31} & \overline{\overline{Z}}_{33} \end{array}\right] \tag{41}$$

From the impedance matrix, the scattering matrix $\overline{\overline{S}}$ of the multilayer structure, defined by:

$$\left[\begin{array}{c} \overline{E}_1^- \\ \hline \overline{E}_3^- \end{array}\right] = \left[\begin{array}{c|c} \overline{\overline{S}}_{11} & \overline{\overline{S}}_{13} \\ \hline \overline{\overline{S}}_{31} & \overline{\overline{S}}_{33} \end{array}\right] \left[\begin{array}{c} \overline{E}_1^+ \\ \hline \overline{E}_3^+ \end{array}\right] \tag{42}$$

can be computed from Eq. 40 for arbitrary imbedding impedances η_1 and η_3:

$$\overline{\overline{S}} = (\overline{\overline{Z}} + \overline{\overline{I}})^{-1} (\overline{\overline{Z}} - \overline{\overline{I}}) \tag{43}$$

where:

$$\overline{\overline{Z}} = \left[\begin{array}{c|c} -\overline{\overline{Z}}_{TM1}^{-1} \overline{\overline{Z}}_{11} & -\overline{\overline{Z}}_{TM1}^{-1} \overline{\overline{Z}}_{13} (\eta_1/\eta_3) \\ \hline \overline{\overline{Z}}_{TM3}^{-1} \overline{\overline{Z}}_{31} (\eta_3/\eta_1) & \overline{\overline{Z}}_{TM3}^{-1} \overline{\overline{Z}}_{33} \end{array}\right] \tag{44}$$

and $\overline{\overline{Z}}_{TMq}$ is the TM wave impedance matrix with diagonal elements $k_{qzn}\eta_q/k_q$. The scattering matrix consists of four sub-matrices $\overline{\overline{S}}_{ij}$. These are the generalized scattering (matrix) coefficients.

With respect to Eqs. 4 and 5, the amplitudes $\overline{\overline{R}}_n$ and $\overline{\overline{T}}_n$ for an incident TM plane wave are:

$$\left[\begin{array}{c} \vdots \\ \overline{R}_{-2} \\ \overline{R}_{-1} \\ \overline{R}_{-0} \\ \overline{R}_1 \\ \overline{R}_2 \\ \vdots \\ \hline \vdots \\ \overline{T}_{-2} \\ \overline{T}_{-1} \\ \overline{T}_{-0} \\ \overline{T}_1 \\ \overline{T}_2 \\ \vdots \end{array}\right] = \overline{\overline{S}} \left[\begin{array}{c} \vdots \\ 0 \\ 0 \\ \eta_1 H_o \\ 0 \\ 0 \\ \vdots \\ \hline \vdots \\ 0 \\ 0 \\ 0 \\ 0 \\ 0 \\ \vdots \end{array}\right] \tag{45}$$

To explicity compute the fields within an arbitrary layer, the coefficients $\overline{C}_l$ for that layer can be found by stepping downward from the top boundary. The recursion is:

$$\overline{C}_{l+1} = \overline{\overline{e}}_{l+1}^{-1}(\Delta z_{l+1})\,\overline{\overline{W}}_{l+1}^{-1}\,\overline{\overline{W}}_l\,\overline{C}_l \tag{46}$$

where for the top layer:

$$\overline{C}_1 = \frac{1}{\eta_1}\overline{\overline{e}}_1^{-1}(\Delta z_1)\,\overline{\overline{W}}_1^{-1}\left[\frac{\overline{\overline{Z}}_{TM1}(\overline{E}_1^+ + \overline{E}_1^-)}{(-\overline{E}_1^+ + \overline{E}_1^-)}\right] \tag{47}$$

and $\overline{E}^-$ is computed via Eq. 42. Equivalently, stepping can be performed from the bottom layer upward. To minimize the accumulated effects of roundoff error, it is best to step from both boundaries ($z = 0$ and $z = -d$) inward to $z = -d/2$.

The above linear multiport formulation has advantages over previous coupled wave formulations [14, 15, 16, 17] in both computational complexity and physical interpretation. By cascading the transmission matrices for L grating layers the number of calculations in the above follows $\sim LN^3$. Formulations for which all boundary conditions between layers are prescribed simultaneously result in complexities of $\sim (LN)^3$. An exception is [17], in which the complexity was reduced by exploiting the sparseness of the boundary condition matrix. However, these formulations obscure the physical nature of the fields. In the linear multiport formulation the electromagnetic fields above and below each layer are simply interpreted as superpositions of reflected and transmitted Floquet harmonics.

Although we have only discussed the TM solution, the TE solution is readily found using duality [24], where $\overline{E}_{TM} \rightarrow \overline{H}_{TE}$, $\overline{H}_{TM} \rightarrow -\overline{E}_{TE}$, and $\epsilon \leftrightarrow \mu$. Note that in the case of a homogeneous layer, the submatrices in $\overline{\overline{A}}$ (Eq. 21) are diagonal, thus the eigenvectors matrix $\overline{\overline{W}}$ is also diagonal, and the eigenvalues are the k_{qzn}. Both the propagator and transmission matrices are diagonal, indicating coupling of only specular space harmonics. This is the familiar case of reflection and transmission from homogeneous layered media.

3 Numerical Solution for a Wedge-Corrugated Absorber

The above coupled wave method has been applied to the case of a wedge-corrugated absorber. The absorber is located in free space, and comprised of an iron-loaded epoxy material with approximate dielectric parameters $\epsilon = 9 - j0.4$ and $\mu = 1 - j0.5$ at millimeter-wave frequencies [26]. The dimensions d and Λ are comparable to the free space electrical wavelength $\lambda = 2\pi/k_1$.

3.1 Discretization Criteria and Power Conservation

The accuracy of the coupled wave solution depends on both the number of layers L and harmonics N. The effect of finite N is twofold: First, the dielectric interface is not modelled by a jump discontinuity in the material constants, but rather by a non-localized oscillatory transition characteristic of an incomplete Fourier reconstruction of a step functions. Second, sudden $x-$directed spatial variations in $\overline{E}$ and $\overline{H}$ are not described. To gain insight on the necessary value of N, we model the unknown field structure in a particular layer by a piecewise-continuous analytic profile. The profile (Fig. 5) is sinusoidal outside the absorber material with a period equal to the incident wavelength λ. Inside the material the field decays exponentially with a decay constant determined by the material's skin depth $1/k_3''$.

A measure of the ability of a finite series of space harmonics to describe this profile can be defined by the ratio of energy in the lowest $2N+1$ Fourier coefficients to the total profile energy. For the model profile, the fractional power versus N is plotted in Fig. 6 for three layer positions: $z_l = 0, -d/2$ and $-d$. When the composite field is primarily exponential in form (corresponding to z_l near zero) a larger number of coefficients is required to achieve an acceptable fraction. For the above absorber material and with $d = 7.5\lambda$ and $\Lambda = 3.75\lambda$ (several electrical wavelengths), $N \geq 20 - 25$ is required to obtain a fractional energy ratio of $\sim 90 - 95\%$. This minimum

required value increases inversely with skin depth and wavelength. However, as N increases, the condition numbers of the propagator matrices increase, and numerical quantization noise begins to render the solution unstable.

Electromagnetic power conservation requires that the incident $z-$directed power flux is equal to the sum of the $z-$directed power fluxes scattered into regions 1 and 3 and the total power absorbed in region 2. The scattered fluxes are determined by integrating over a full period and representative width w:

$$\int_0^w \int_0^\Lambda \tfrac{1}{2} Re\{\overline{E}_1^-(x, z=0) \times \overline{H}_1^{-*}(x, z=0)\} \cdot \hat{z}\, dx\, dy \tag{48}$$

$$\int_0^w \int_0^\Lambda \tfrac{1}{2} Re\{\overline{E}_3^-(x, z=-d) \times \overline{H}_3^{-*}(x, z=-d)\} \cdot (-\hat{z})\, dx\, dy \tag{49}$$

The power absorbed in the l^{th} layer of region 2 is:

$$\int_{z_{l+1}}^{z_l} \int_0^w \int_0^\Lambda \frac{1}{2} k_o \eta_o \left[Im\{\epsilon_l(x,z)\} |\overline{E}_{2l}(x,z)|^2 + Im\{\mu_l(x,z)\} |\overline{H}_{2l}(x,z)|^2 \right] dx\, dy\, dz \tag{50}$$

Calculations based on Eqs. 48-49 show agreement with power conservation to within one part in $\sim 10^6$. These calculations serve to detect the effects of numerical quantization noise and illustrate the accuracy of the numerical implementation. The power conservation results are independent of the number of harmonics used in the analysis.

Convergence of the total reflected power is monotonically increasing, and occurs near $N \approx 20 - 30$. This is expected, since harmonic numbers at least this large are required for the dielectric interface model to appear discontinuous on the scale of field variation. For smaller N, the dielectric interface appears "fuzzy" on this scale, thus yielding a decrease in the reflected energy. The phenomenon is analogous to the decrease in reflectivity provided by a tapered matching section between transmission lines of different impedance.

Due to the suitability of complex exponentials for describing both oscillatory and damped field variations in z, the required number of layers is not restrictive. Typically, discretization with $\Delta z \approx \lambda/10$ provides stable reflectivity values.

3.2 Graphical Visualization of Fields

A graphical display of the fields around and within the wedge absorber has been developed to provide a qualitative verification of the accuracy of the coupled wave solution. Figs. 7a and b show electric field streamlines for TM incidence with $\theta_i = 30^0$, $d = 7.5\lambda$ and $\Lambda = 3.75\lambda$. Discretization was performed using $L = 19$ and $N = 25$; no numerical quantization noise is apparent. The shadow region below and to the right of the wedge peaks can be clearly seen in Fig. 7a, consistent with geometric optics theory. Little specular reflection from the illuminated wedge face is apparent. This is expected since the angle of incidence relative to the face is close to Brewster's angle for TM waves[1].

A magnified view of the wedge tip region (Fig. 7b) reveals that the tangential-field boundary conditions are satisfied and that the field attenuation within the absorber is consistent with the skin depth. Furthermore, there is evidence of surface polarization charge ρ_{sp} near the wedge tip, where $\rho_{sp} = -\epsilon_o \hat{n} \cdot [\overline{P}_1 - \overline{P}_2]$. Here, $\overline{P}(x,z) = \epsilon_o[\epsilon_l(x,z) - 1]\overline{E}_{2l}(x,z)$ is the electric polarization vector for outside (1) and inside (2) the absorber surface and $\hat{n}$ is the outward-pointing surface normal. The ρ_{sp} on the two opposing faces of a wedge forms a dipole surface charge wave that travels down the wedge. This dipole surface charge wave acts as a travelling-wave radiator, and is the principle cause of scattering from the wedge peaks.

3.3 Comparisons with Integral Equation Formulation

Results from the coupled wave formulation and an integral equation formulation using a periodic Green's function (PGF) have been compared for consistency. The PGF formulation, detailed elsewhere [7], determines the fields in each region by numerically solving four integral equations, one each for the electric and magnetic vector potential functions on both sides of the wedge boundary. Because of the Floquet condition,

[1]Since η_1/η_3 is complex, there is strictly no angle of total transmission. However, the specular TM reflection coefficient exhibits a minimum at $\sim 70^o$ local incidence.

the integration is performed over one wedge period. The integrals involve unknown equivalent electric and magnetic currents defined along the wedge boundary, and known free-space Green's functions for both sides of the wedge boundary. The method of moments is used to compute the unknown currents, and subsequently, the diffracted fields.

The amplitudes of the zeroth and first-order reflected and transmitted magnetic fields obtained using each of the two methods are shown for a non-absorbing periodic wedge surface ($\epsilon_3 = 2.5, \mu_3 = 1.0$) in Fig. 8. An incident TM plane wave with $\theta_i = 30^\circ$ and $\Lambda = 1.0\lambda$ is used. In all cases, the illustrated amplitudes represent propagating waves. Both approaches agree well for depths up to 1.5λ. However, the coupled wave technique has the advantage of being directly applicable to inhomogeneous dielectric substrates.

4 Laboratory Scattering Measurements

Millimeter-wave bistatic scattering measurements of two wedge-corrugated absorber samples were performed to verify the coupled wave theory. Both absorbers consist of Emerson-Cumming CR-114 iron-impregnated epoxy cast to the dimensions in Table 6. The bistatic measurements were made using a focussed-lens scattering range. Deconvolution of the angular sensitivity pattern of the scattering range was performed using the CLEAN algorithm.

4.1 Measurement System

The scattering range consists of identical focussed-lens transmitting and receiving antennas interfaced to a Hewlett-Packard model 8510 network analyzer system 9. The HP 8510 system consists of a display/processor unit, two HP 8341 phase-locked microwave sources and an external S-parameter test set. The signal from the first

(transmitter) source is amplified and up-converted by a W-band mixer, then radiated. A directional coupler permits a portion of this signal to be downconverted and used as a reference for complex S_{21} measurements. The received signal is similarly down-converted using the phase-locked signal from the second (receiver) source. The system provides a dynamic range of $\sim$ 55 dB over the band 75-100 GHz.

The two focussed-lens antennas consist of standard gain horns and rexolite lenses. Each are mounted on radial booms that rotate about a common axis lying in the plane of the sample's surface. The configuration produces a focussed spot with a diameter of $\sim$ 6 cm on the sample surface. The range permits both co- and cross-polarized bistatic scattering measurements for both TE- and TM-incident polarizations.

Bistatic reflection data were measured for a range of θ_i from 20° to 70° in 10° increments. Due to a minumum 40° angular separation between each boom (for mechanical reasons), the corresponding range of θ_s was constrained to be $40° - \theta_i \leq \theta_s \leq 70°$. Although both magnitude and phase measurements were made, positioning errors rendered the phase information unusable. Bistatic data were also measured for a flat aluminum plate; this data was subsequently used for calibration and deconvolution purposes.

4.2 CLEAN Algorithm

The measured reflectivity amplitude S^M is considered to be a convolution of the sample's angular reflectivity pattern S^S and the angular response S^P of the measurement system:

$$S^M_{\beta\alpha}(\theta_i, \phi_i; \theta_s, \phi_s) = \int_0^{2\pi} \int_0^{\pi/2} S^P_{\beta\alpha}(\theta'_s, \pi - \phi'_s; \theta_s, \phi_s)\, S^S_{\beta\alpha}(\theta_i, \phi_i; \theta'_s, \phi'_s)\, \sin\theta'_s\, d\theta'_s\, d\phi'_s \tag{51}$$

where α, β denote the transmitter and receiver polarizations (respectively), and are either TE or TM. Due to the relatively broad angular response of the measurement

system, the effects of S^P must be considered. For identical transmitter and receiver polarizations, S^P is obtained from the flat aluminum plate measurements. [2] Due to a lack of usable phase information, we have modelled the above observation process as a superposition of power contributions:

$$|S^M_{\beta\alpha}(\theta_i, \phi_i; \theta_s, \phi_s)|^2 = \int_0^{2\pi} \int_0^{\pi/2} |S^P_{\beta\alpha}(\theta'_s, \pi - \phi'_s; \theta_s, \phi_s)|^2 \, |S^S_{\beta\alpha}(\theta_i, \phi_i; \theta'_s, \phi'_s)|^2 \sin\theta'_s \, d\theta'_s \, d\phi'_s \tag{52}$$

In the above, we assume that contributions to the received power from all angles are incoherent.

In order to compare the bistatic scattering pattern to the computed Floquet harmonic amplitudes, deconvolution of the probe function $|S^P|^2$ was performed using the CLEAN algorithm [21, 22]. Developed for use in radioastronomical imaging, this iterative technique is well suited for reconstruction of point-like source functions from spatially low-pass filtered measurements. Since the angular reflectivity of the absorber samples consists of a discrete set impulses (each corresponding to a propagating Floquet harmonic), CLEAN is particularly useful. Further, CLEAN allows deconvolution of space-varying probe functions, as encountered here.

The algorithm begins by initializing the cleaned array $|S^S|^2$ with zeroes, and the residual and probe arrays with $|S^M|^2$ and $|S^P|^2$, respectively (Fig. 10). The peak in the current residual pattern is found, and a scaled probe pattern is subtracted from the residual at this location. The scaling factor is an empirical loop gain parameter selected to be in the range 0.1-0.5. The remainder from this operation replaces the residual pattern, and a positive impulse of amplitude equal to the scaling factor is added to the CLEANed array at the location of the peak. The loop continues until all peaks in the residual pattern are smaller than the standard deviation of the measurement noise amplitude, which was 50 dB below the peak specular reflectivity from the aluminum plate.

[2] Due to sensitivity limitations, our measurements were restricted to cases of like polarization. For differing transmitter and receiver polarizations, S^P could be obtained using a quarter-wave plate in series with the flat reflector.

5 Results and Applications

5.1 Comparison of Measurements and Calculations

The deconvolved reflectivities for the J and K samples were compared to coupled wave calculations of the power in the reflected Floquet harmonics. The comparisons were performed at a midband frequency of 89 GHz ($\lambda = 3.37$ mm). The calculations used $\epsilon = 9 - j0.4$ and $\mu = 1 - j0.5$. The results of the comparisons are shown in Figs. 12 and 11 for TE and TM incidence, respectively.

In most cases, the CLEANed data ($|S^S|^2$) shows both specular ($n = 0$) and diffuse ($n \neq 0$) Floquet harmonics at approximately the expected angular locations (as determined by Eqs. 6 and 7). However, in some cases (due to measurement errors) CLEANing results in either additional (spurious) harmonics (Figs. 12b and 11a) or missing harmonics (Fig. 11b).

Referring to Eq. 45, the calculated reflectivity for the n^{th} Floquet harmonic is:

$$r_{n\alpha} = |\overline{R}_n|^2 \frac{\cos\theta_{sn}}{\cos\theta_i} \tag{53}$$

with $\eta_1 H_o = 1$. As expected for surfaces with impedances $\eta_3 < \eta_1$, the TE harmonic amplitudes are significantly larger than the corresponding TM amplitudes. Accordingly, TM is the desired polarization for best performance from wedge absorbers having $\epsilon' > \mu'$.

The CLEANed reflectivities generally corroborate the coupled wave calculations, although the measurements are usually higher by 3-10 dB. A large portion of this discrepancy can be ascribed to measurement accuracy. Although the short-term repeatability of the measurements was better than 0.5 dB, fluctuations of up to ~ 3 dB were observed to be caused by mechanical misalignment.

5.2 Sensitivity to Assumed Dielectric Parameters

We can determine the uncertainty in the calculated harmonic reflectivities using computed sensitivity functions:

$$(\delta r_{n\alpha})^2 = \left(\frac{\partial r_{n\alpha}}{\partial \epsilon'}\right)^2 (\delta\epsilon')^2 + \left(\frac{\partial r_{n\alpha}}{\partial \epsilon''}\right)^2 (\delta\epsilon'')^2 + \left(\frac{\partial r_{n\alpha}}{\partial \mu'}\right)^2 (\delta\mu')^2 + \left(\frac{\partial r_{n\alpha}}{\partial \mu''}\right)^2 (\delta\mu'')^2 \tag{54}$$

The $\delta\epsilon', \delta\epsilon'', \delta\mu', \delta\mu''$ are uncertainties the absorber material's dielectric parameters, and are each estimated to be ~ 0.2. For our samples and incidence angles, the third term accounting for uncertainty in μ' dominates in both TE and TM cases, [3] resulting in $\delta r_{n\alpha} \tilde{<} 2$ dB for any n. This uncertainty is hypothesized to account for some of the discrepancy between the computed and CLEANed reflectivity amplitudes.

5.3 Wideband Absorber Design

The design of wideband absorbing structures is based on minimizing the total reflectivity r_α, defined as [27]:

$$r_\alpha(\theta_i, \phi_i) = \frac{1}{4\pi} \int_0^{2\pi} \int_0^{\pi/2} \sum_\beta \gamma_{\beta\alpha}(\theta_i, \phi_i; \theta_s \phi_s) \sin\theta_s \, d\theta_s \, d\phi_s \tag{55}$$

where α, β are either TE or TM and θ_i, ϕ_i denote the observation direction. In the above, $\gamma_{\beta\alpha}(\theta_i, \phi_i; \theta_s, \phi_s)$ is the surface bistatic scattering function for incident radiation of polarization α scattered into radiation of polarization β. For periodic surfaces $\gamma_{\beta\alpha}$ consists of a finite sum of delta functions, one for each propagating reflected harmonic. In terms of Eq. 4:

$$\gamma_{\beta\alpha}(\theta_i, \phi_i; \theta_s, \phi_s) = 4\pi \sum_{k'_{zn} \neq 0} \delta(\cos\theta_s - \cos\theta_{sn}) \delta(\phi_s - \phi_{sn}) |\overline{R}_n \cdot \hat{e}_\beta|^2 \frac{\cos\theta_{sn}}{\cos\theta_i} \tag{56}$$

where the incident wave is of polarization α and amplitude $E_o = 1$, and $\hat{e}_\beta$ is a unit vector in the direction of the electric field for β-polarization. It follows from Eq. 55

[3] For the TM case, the coupling of the incident wave into the dielectric is more strongly influenced by μ' than ϵ' since $\overline{H}$ is parallel to the edges. For the TE case, the opposite would be expected. However, since $\epsilon' \approx 9$ and $\mu' \approx 1$, the relative effect of changing ϵ' by 0.2 is smaller than that of changing μ' by 0.2.

that:

$$r_\alpha(\theta_i, \phi_i) = \sum_{k'_{zn} \neq 0} |\overline{R}_n|^2 \frac{\cos\theta_{zn}}{\cos\theta_i} \tag{57}$$

For a perfectly reflecting surface, $r_\alpha = 1$.

Reflectivity calculations for a wedge absorber with normal TM incidence ($\theta_i = 0^\circ$), $\epsilon = 9 - j0.4$ and $\mu = 1 - j0.5$ and varying absorber dimensions have been computed using the coupled wave technique (Fig. 13). The number of harmonics and layers was 27 and 120, respectively. The results show generally decreasing reflectivity as the electrical depth of the structure increases, although the reflectivity tends to saturate for depths greater than $\sim 1 - 2\ \Lambda$. This can be explained as follows: Increasing depths increase the length of the inhomogeneous transition region between free space and the bulk absorber. This improves the match between these regions in the same manner provided by a tapered matching section between transmission lines of different impedance. The saturation is hypothesized to be the result of scattering by the tips of the absorber wedges. This mechanism appears to impose a lower limit on the reflectivity of a wedge periodic structure.

In addition to the overall decreasing reflectivity, some periodic behavior can be seen, particularly for d/Λ from 0.25 to 1.0. This behavior can be explained by noting that sharp increases of reflectivity tend to occur at integral values of Λ/λ, corresponding precisely to the onset of additional propagating Floquet harmonics. Such harmonics carry additional power away from the interface. In the limit of a flat surface, the reflectivity converges to the specular value (-6.2 dB), as required.

The calculations suggest that wedge-type absorbers with total TM reflectivities less than -30 dB (0.001) and decade (or greater) bandwidths can be obtained by choosing $d/\Lambda \geq 2$. Although these calculations assumed specific dielectric values, the reflectivities for absorbers of slightly different dielectric constitution can be estimated using the sensitivity parameters in Table 6, where:

$$r_\alpha(\epsilon + \delta\epsilon, \mu + \delta\mu) \approx r_\alpha(\epsilon, \mu) + \frac{\partial r_\alpha}{\partial \epsilon'}\delta\epsilon' + \frac{\partial r_\alpha}{\partial \epsilon''}\delta\epsilon'' + \frac{\partial r_\alpha}{\partial \mu'}\delta\mu' + \frac{\partial r_\alpha}{\partial \mu''}\delta\mu'' \quad (dB) \tag{58}$$

The listed sensitivitiy parameters were obtained numerically by computing divided differences. In the above, ϵ'' and μ'' are positive for lossy media.

6 Summary

Linear N-port analysis along using coupled wave theory provides an efficient numerical method for computing the fields both within and scattered from a lossy periodic structure. Reflectivities computed using this method compare favorably to measured laboratory data after deconvolution using the CLEAN algorithm. Discrepancies in the comparison are ascribed primarily to measurement uncertainty. The coupled wave reflectivities compare very well with calculations based on an integral equation formulation using a periodic Green's function. A distinct advantage of the coupled wave method over Green's function methods is its ready applicability to arbitrary periodic grating structures and otherwise inhomogeneous periodic dielectric materials. This includes structures consisting of several corrugated layers of different material and periodic dielectric structures containing voids.

In principle, the coupled wave method is applicable for arbitrary dielectric material parameters. However, for materials with skin depths that are much smaller than the wavelength (e.g., good conductors), a large number of harmonics are required to describe the field variations. In this case, the the coupled wave method requires the inversion of large ill-conditioned matrices, resulting in numerical noise in the solution. This limitation can be surmounted by higher arithmetic precision, but at increased computational expense. Alternate noise mitigation methods include least-squares boundary matching techniques (e.g., [28]) and ad-hoc elimination of decayed harmonics from layers in which they are known *a-priori* to be negligible [20].

Using the coupled wave method the reflectivity of representative wedge-corrugated absorbers has been computed. By proper selection of the pitch and depth the total TM reflectivity at normal incidence can be reduced to lower than -30 dB over a decade

in bandwidth. It is the total reflectivity, rather than the retroreflectivity, that is important in the design of microwave calibration targets. Additional requirements are that the temperature distribution within the target be precisely known; the problem of the temperature distribution within a microwave calibration target and its effect on the thermal emission are being addressed separately.

Some straightforward extensions of the coupled wave theory follow from the above formulation. These includes the obvious cases for which the grating vector is not in the plane of incidence ($\phi \neq 0$) and for which the surface is periodic in two dimensions. Other innovative applications include scattering from dielectric extrusions using a coupled cylindrical wave formulation and scattering from an arbitrary dielectric object using a coupled spherical wave formulation [29]).

Acknowledgements-The authors acknowledge Markus Bliesener for performing the power conservation analysis, Parag Doshi and Paul Friedrich for assistance in the laboratory measurements, Brian Poszgay for writing the field-visualization software, and Dr. A.F. Peterson of Georgia Tech for helpful discussions. This work has been supported by the Georgia Institute of Technology and NASA Grants NAG 5-1332 and NAG 5-1490.

Table 1: Dimensions of wedge-corrugated absorber samples used in the laboratory bistatic measurements.

Sample	Λ	d
J	3.2	6.5
K	12.5	25.4

Table 2: Sensitivity of total TM reflectivity with respect to dielectric parameters (dB/unit) for normal incidence. The mean dielectric parameters are $\epsilon = 9 - j0.4$ and $\mu = 1 - j0.5$.

	$\Lambda = 0.5\lambda$		$\Lambda = \lambda$		$\Lambda = 2\lambda$	
Quantity	$d/\Lambda = 1$	$d/\Lambda = 4$	$d/\Lambda = 1$	$d/\Lambda = 4$	$d/\Lambda = 1$	$d/\Lambda = 4$
r_{TM} (dB)	-35.1	-37.7	-27.3	-40.9	-28.6	-33.5
$\frac{\partial r_{TM}}{\partial \epsilon'}$	0.90	0.25	0.68	-0.38	0.45	0.45
$\frac{\partial r_{TM}}{\partial \epsilon''}$	-4.01	0.14	0.09	-0.30	-0.72	0.29
$\frac{\partial r_{TM}}{\partial \mu'}$	-68.6	-3.78	-6.09	-10.57	-11.4	-2.70
$\frac{\partial r_{TM}}{\partial \mu''}$	-11.7	4.66	-6.88	2.77	-4.61	2.69

Figure 1: Periodic surface scattering geometry for an obliquely incident, arbitrarily polarized plane wave.

Figure 2: Schematic diagram illustrating the implications of the Floquet condition and phase matching on propagating and evanascent plane waves in the upper and lower half spaces.

Figure 3: Discretization of the periodic region (2) into N layers for the coupled-wave analysis. Each layer is modelled as a linear multi-port network with an associated transmission matrix. The scattering problem is solved by cascading the individual layers.

Figure 4: Schematic diagram of a single grating layer, illustrating incident and scattered waves. The scattering behavior of each grating layer is described using a transmission matrix by considering the layer to be a linear multiport network.

Figure 5: Piecewise-continuous analytic profile used to model the field structure in a period layer.

Figure 6: Fractional power in the incomplete Fourier series representation of the piecewise-continuous analytic profile.

Figure 7: Electric field streamlines for a TM plane wave obliquely incident on a wedge absorber: (a) full view, showing geometrical shadow (below dashed lines) and (b) magnified view of a wedge tip, showing surface polarization charge density. The parameters are $\theta_i = 30°$, $d = 7.5\lambda$, $\Lambda = 3.75\lambda$, $\epsilon = 9 - j0.4$ and $\mu = 1 - j0.5$.

Figure 8: Comparison of transmitted and reflected harmonic amplitudes (arbitrary units) for each of two methods: coupled wave and periodic Green's function. The magnetic field magnitudes for the indicated propagating harmonics are plotted.

Figure 9: Schematic diagram of the focussed-lens millimeter-wave scattering range.

Figure 10: Functional block diagram of the CLEAN algorithm.

Figure 11: Comparisons of measured data and coupled-wave calculations for wedge absorbers with TM incidence and $\theta_i = 60°$: (a) J sample, and (b) K sample.

Figure 12: Comparisons of measured data and coupled-wave calculations for wedge absorbers with TE incidence and $\theta_i = 60°$: (a) J sample, and (b) K sample.

Figure 13: Wideband TM reflectivity vs. period Λ for wedge absorbers of varying depth d. The calculations used the coupled wave method.

References

[1] Bucci, O.M., and G. Franceschetti, "Scattering from Wedge-Tapered Absorbers", *IEEE Trans. Ant. Prop.*, vol. 19, no. 1, pp. 96-104, January, 1971.

[2] Waterman, P.C., "Scattering by Periodic Surfaces", *J. Acoustic. Soc. America*, vol. 57, no. 4, pp. 791-802, 1975.

[3] Uretsky, J.L., "The Scattering of Plane Waves from Periodic Surfaces", *Ann. Phys.*, vol. 33, pp. 400-427, 1965.

[4] Millar, R.F., "On the Rayleigh Assumption in Scattering by a Periodic Surface", *Proc. Camb. Phil. Soc.*, vol. 65, pp. 773-791, 1969.

[5] van den Berg, P.M., and J.T. Fokkema, "The Rayleigh Hypothesis in the Theory of Reflection by a Grating", *J. Opt. Soc. Am.*, vol. 69, no. 1, pp. 27-31, January 1979.

[6] Janaswamy, R., "Oblique Scattering from Lossy Periodic Surfaces with Applications to Anechoic Chamber Absorbers", *IEEE Trans. Ant. Prop.*, vol. 40, no. 2, pp. 162-169, February, 1992.

[7] Peterson, A.F., "Integral Equation Formulation for Scattering from Continuous or Discrete Dielectric Targets Exhibiting One-dimensional Periodicity", *International Journal of Electronics and Communications (AEÜ)*, vol. 46, no. 5, pp. 336-342, 1992.

[8] Yang, C, W.D. Burnside, and R.C. Rudduck, "A Periodic Moment Method Solution for TM Scattering from Lossy Dielectric Bodies with Application to Wedge Absorber", *IEEE Trans. Ant. Prop.*, vol. 40, no. 6, pp. 652-659, June 1992.

[9] Moaveni, M.K., "Plane Wave Diffraction by Dielectric Gratings, Finite-Difference Formulation", *IEEE Trans. Ant. Prop.*, vol. 37, no. 8, pp. 1026-1031, August, 1989.

[10] Peterson, A.F., "An Outward-Looking Differential Equation Formulation for Scattering from One-Dimensional Periodic Diffraction Gratings", submitted for publication in *Electromagnetics*, 1992.

[11] Gaylord, T.K., and M.G. Moharam, "Analysis and Applications of Optical Diffraction by Gratings", *Proc. IEEE*, vol. 73, no. 5, pp. 894-937, May, 2985.

[12] Benali, A., J. Chandezon, and J. Fontaine, "A New Theory for Scattering of Electromagnetic Waves from Conducting or Dielectric Rough Surfaces", *IEEE Trans. Ant. Prop.*, vol. 40, no. 2, pp. 141-148, February, 1992.

[13] Dewitt, B.T., and W.D. Burnside, "Electromagnetic Scattering by Pyramidal and Wedge Absorber", *IEEE Trans. Ant. Prop.*, vol. 36, no. 7, pp. 971-984, July 1988.

[14] Moharam, M.G., and T.K. Gaylord, "Diffraction Analysis of Dielectric Surface-Relief Gratings", *J. Opt. Soc. Am.*, vol. 72, no. 10, pp. 1385-1392, October, 1982.

[15] Moharam, M.G., and T.K. Gaylord, "Rigorous Coupled-Wave Analysis of Grating Diffraction- E-mode Polarization and Losses", *J. Opt. Soc. Am.*, vol. 73, no. 4, pp. 451-455, April, 1983.

[16] Rokushima, K., and J. Yamakita, "Analysis of Anisotropic Dielectric Gratings", *J. Opt. Soc. Am.*, vol. 73, no. 7, pp. 901-908, July, 1983.

[17] Moharam, M.G., and T.K. Gaylord, "Three-Dimensional Vector Coupled-Wave Analysis of Planar-Grating Diffraction", *J. Opt. Soc. Am.*, vol. 73, no. 9, pp. 1105-1112, September, 1983.

[18] Gasiewski, A.J., and D.M. Jackson, "Electromagnetic Scattering from Microwave Absorbers: Laboratory Verification of the Coupled Wave Theory", *Proc. 1992 APS International Symposium*, pp. 412-415, presented in Chicago, Illinois, July 18-25, 1992.

[19] Cwik, T., and R. Mittra, "The Cascade Connection of Planar Periodic Surfaces and Lossy Dielectric Layers to Form an Arbitrary Periodic Screen", *IEEE Trans. Ant. Prop.*, vol. 35, no. 12, pp. 1397-1405, December, 1987.

[20] Hall, R.C., R. Mittra, and K.M. Mitzner, "Analysis of Multilayered Periodic Structures Using Generalized Scattering Matrix Theory", *IEEE Trans. Ant. Prop.*, vol. 36, no. 4, pp. 511-517, April, 1988.

[21] Högbom, J.A., "Aperture Synthyesis with a Non-Regular Distribution of Interferometer Baselines", *Astron. Astrophys. Suppl.*, vol. 15, pp. 417-426, 1974.

[22] Thompson, A.R., J.M. Moran, and G.W. Swenson, *Interferometry and Synthesis in Radio Astronomy*, Malabar, FL: Krieger Publishing Co., 1991.

[23] Morse, P.M., and H. Feshbach, *Methods of Theoretical Physics, Vol I*, New York: McGraw-Hill, 1953.

[24] Collin, R.E., *Field Theory of Guided Waves (2^{nd} ed.)*, New York: IEEE Press, 1991.

[25] Chew, W.C., *Waves and Fields in Inhomogeneous Media*, New York: Van Nostrand Reinhold, 1990.

[26] "Eccosorb MF Machinable Rod, Bar and Sheet Stock with Lossy Magnetic Loading", Emerson and Cuming Technical Bulletin TB 2-6/4-82, April, 1982.

[27] Tsang, L., J.A. Kong and R.T. Shin, *Theory of Microwave Remote Sensing*, New York: John Wiley and Sons, 1985.

[28] Yamakita, J., and K. Rokushima, "Modal Expansion Method for Dielectric Gratings with Rectangular Grooves", *Proc. Soc. Photo. Instr. Eng.*, vol. 503, pp. 239-243, presented at San Diego, CA, Aug 21-23, 1984.

[29] Gasiewski, A.J., and M. Bliesener, "Coupled Spherical-Wave Approach to Scattering from Dielectric Objects" *Proc. 1992 URSI Radio Science Meeting*, p. 514, presented in Chicago, Illinois, July 18-25, 1992.

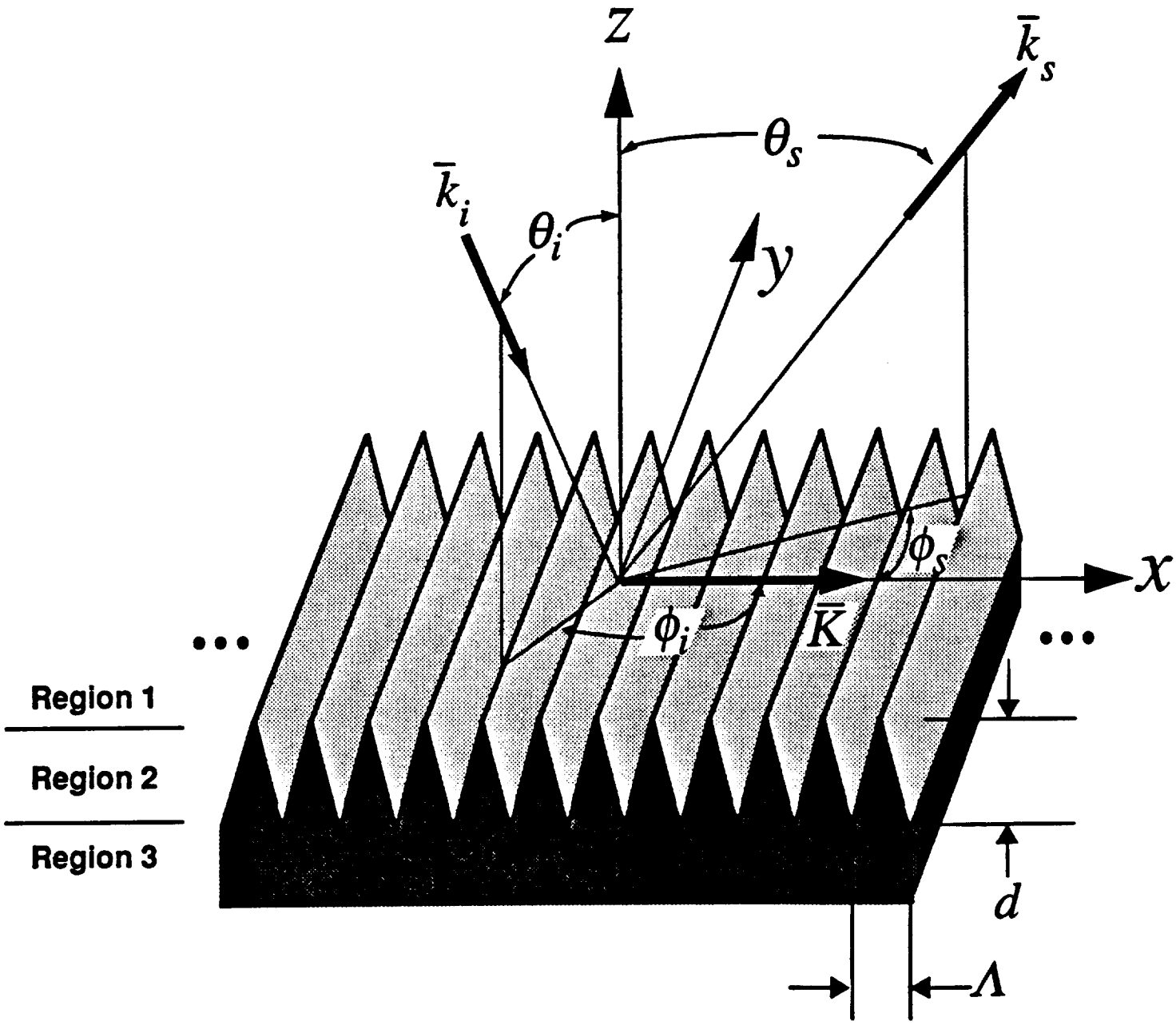
z
$\bar{k}_s$
θ_s
$\bar{k}_i$
θ_i
y
x
ϕ_s
ϕ_i
$\bar{K}$
Region 1
Region 2
Region 3
d
Λ

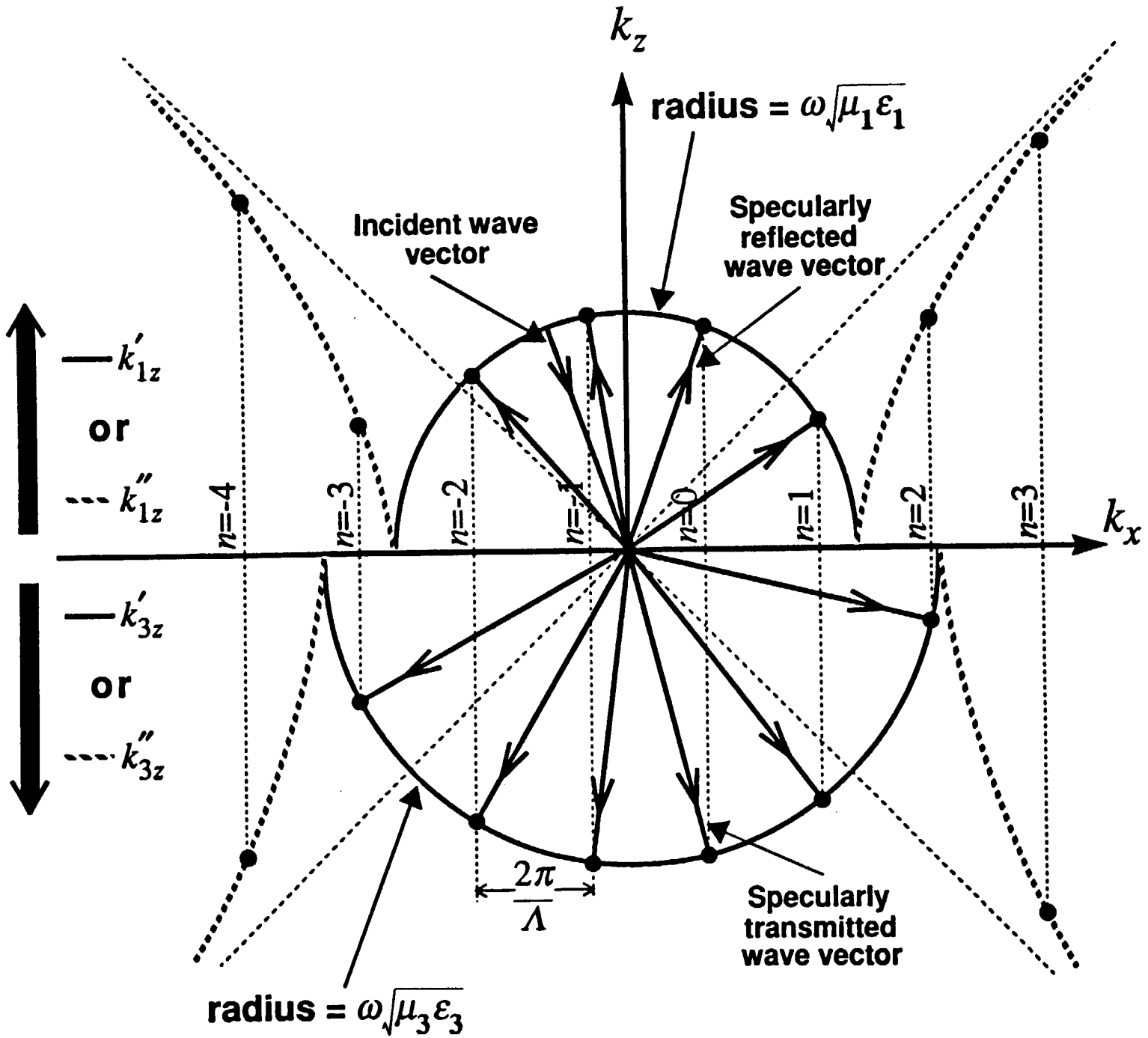
k_z
radius = $\omega\sqrt{\mu_1\varepsilon_1}$
Incident wave vector
Specularly reflected wave vector
k'_{1z}
or
k''_{1z}
k'_{3z}
or
k''_{3z}
n=-4
n=-3
n=-2
n=-1
n=0
n=1
n=2
n=3
k_x
$\frac{2\pi}{\Lambda}$
Specularly transmitted wave vector
radius = $\omega\sqrt{\mu_3\varepsilon_3}$

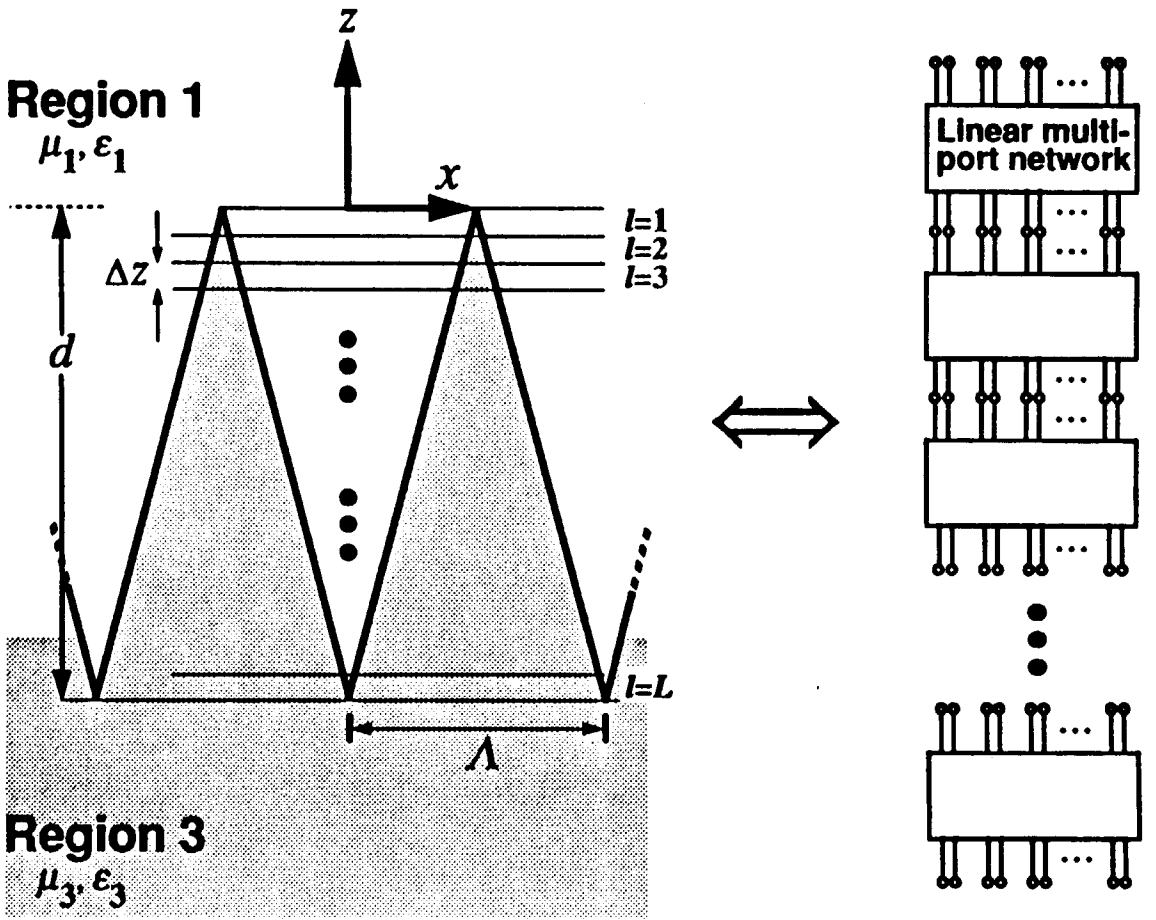
Region 1
μ_1, ε_1
z
x
l=1
l=2
l=3
Δz
d
l=L
Λ
Region 3
μ_3, ε_3
Linear multi-port network

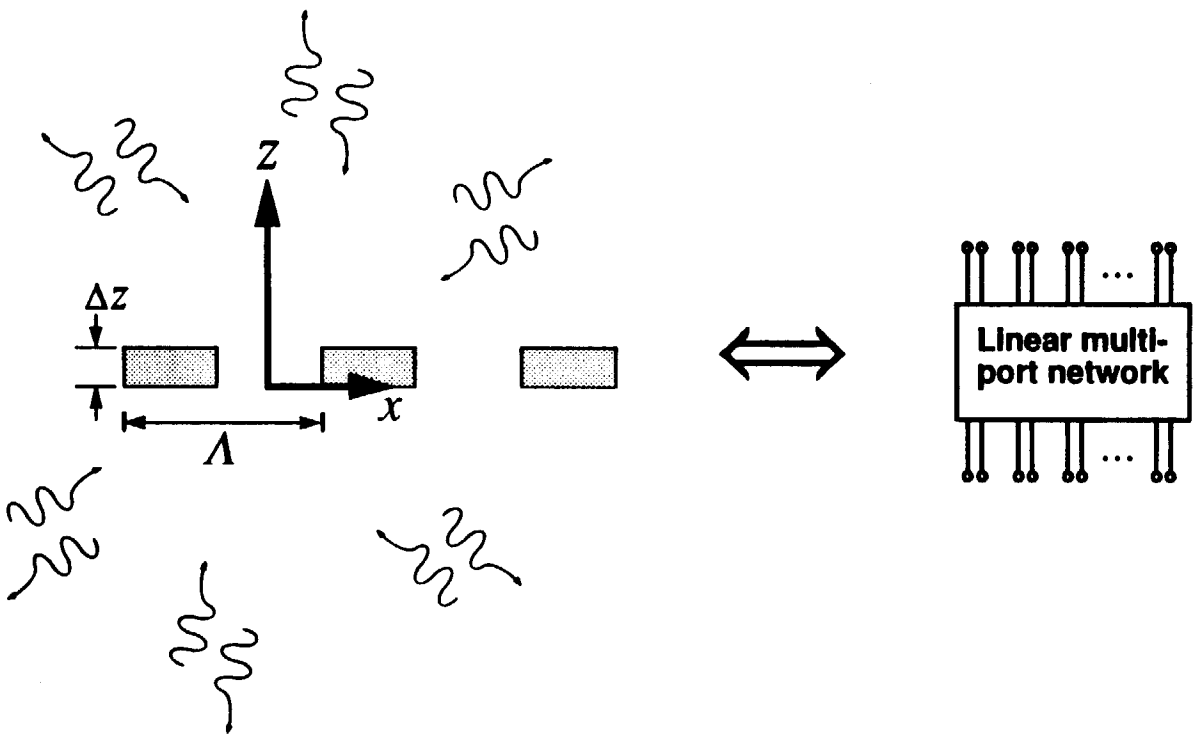
z
Δz
x
Λ
Linear multi-
port network

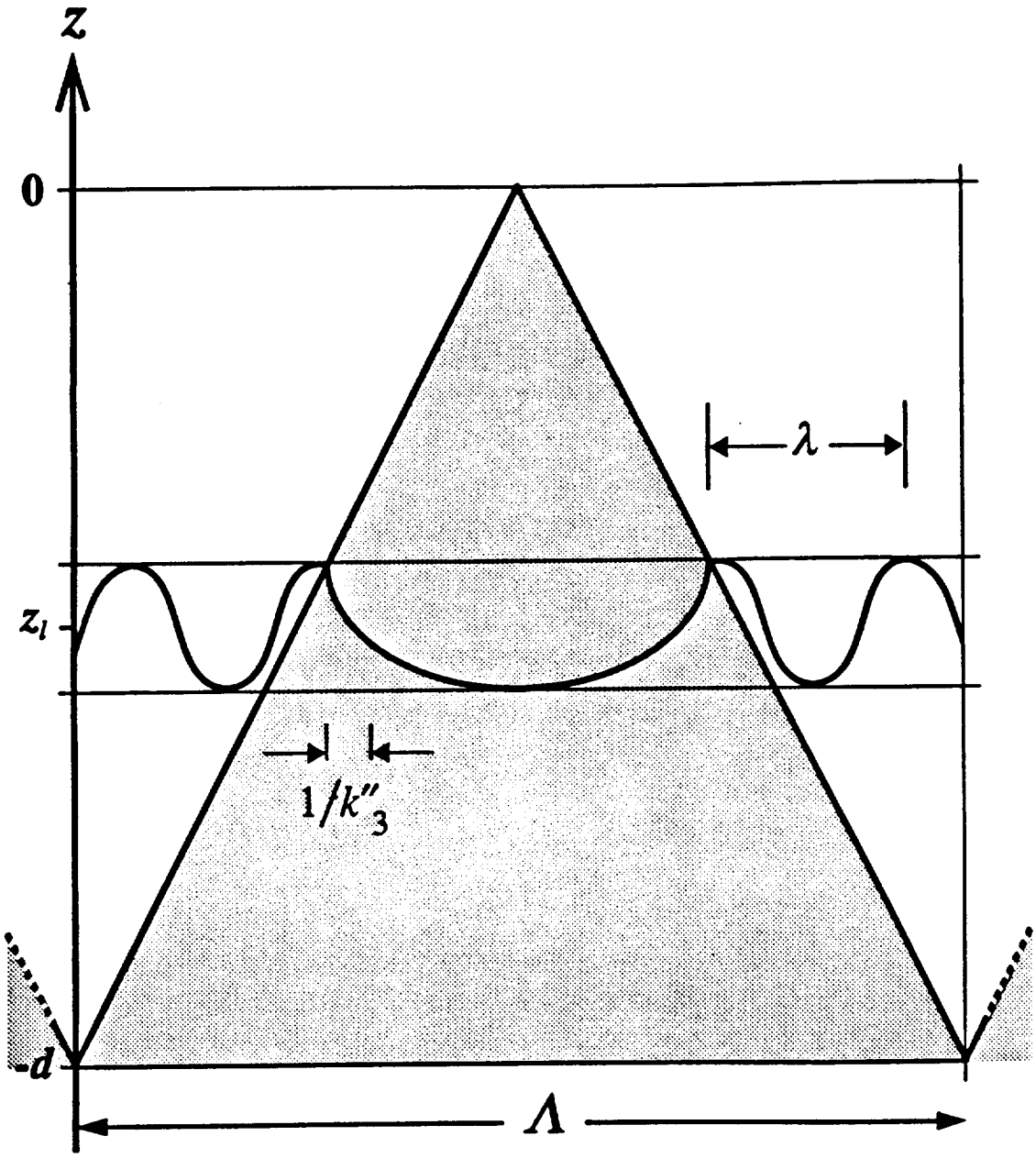
z
0
λ
z_l
$1/k''_3$
-d
Λ

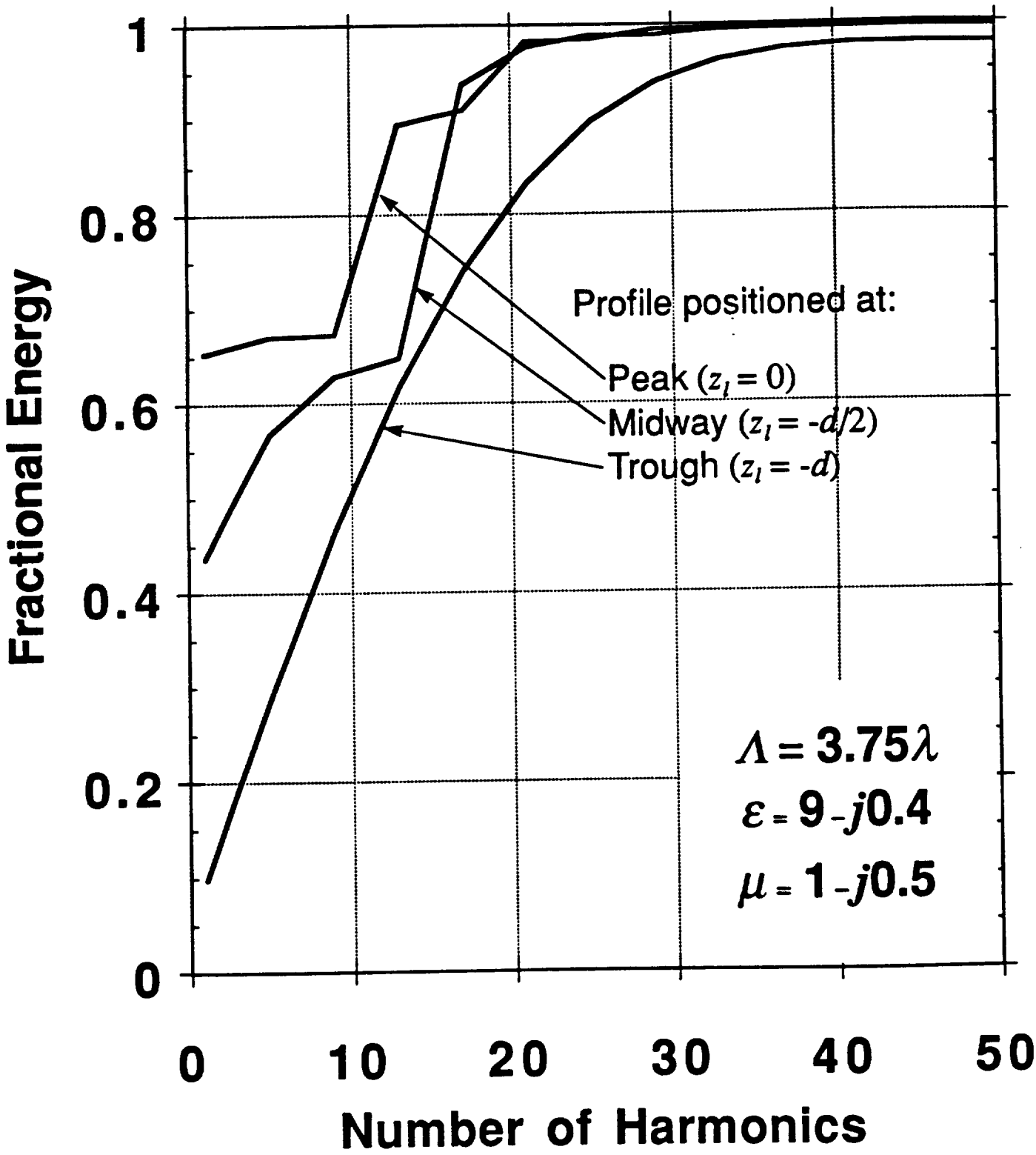
Fractional Energy
1
0.8
0.6
0.4
0.2
0
Profile positioned at:
Peak ($z_l = 0$)
Midway ($z_l = -d/2$)
Trough ($z_l = -d$)
$\Lambda = 3.75\lambda$
$\varepsilon = 9 - j0.4$
$\mu = 1 - j0.5$
0
10
20
30
40
50
Number of Harmonics

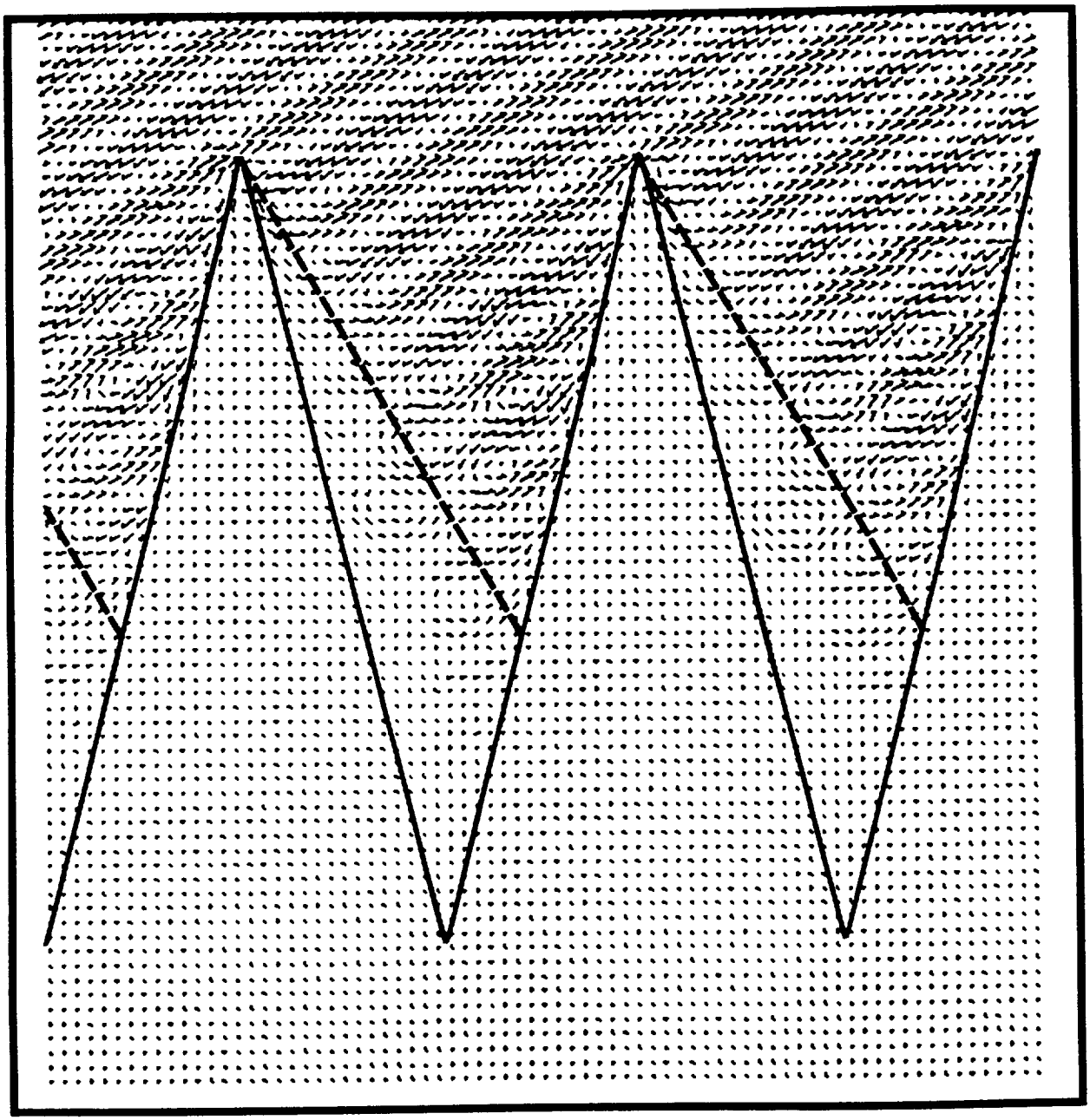

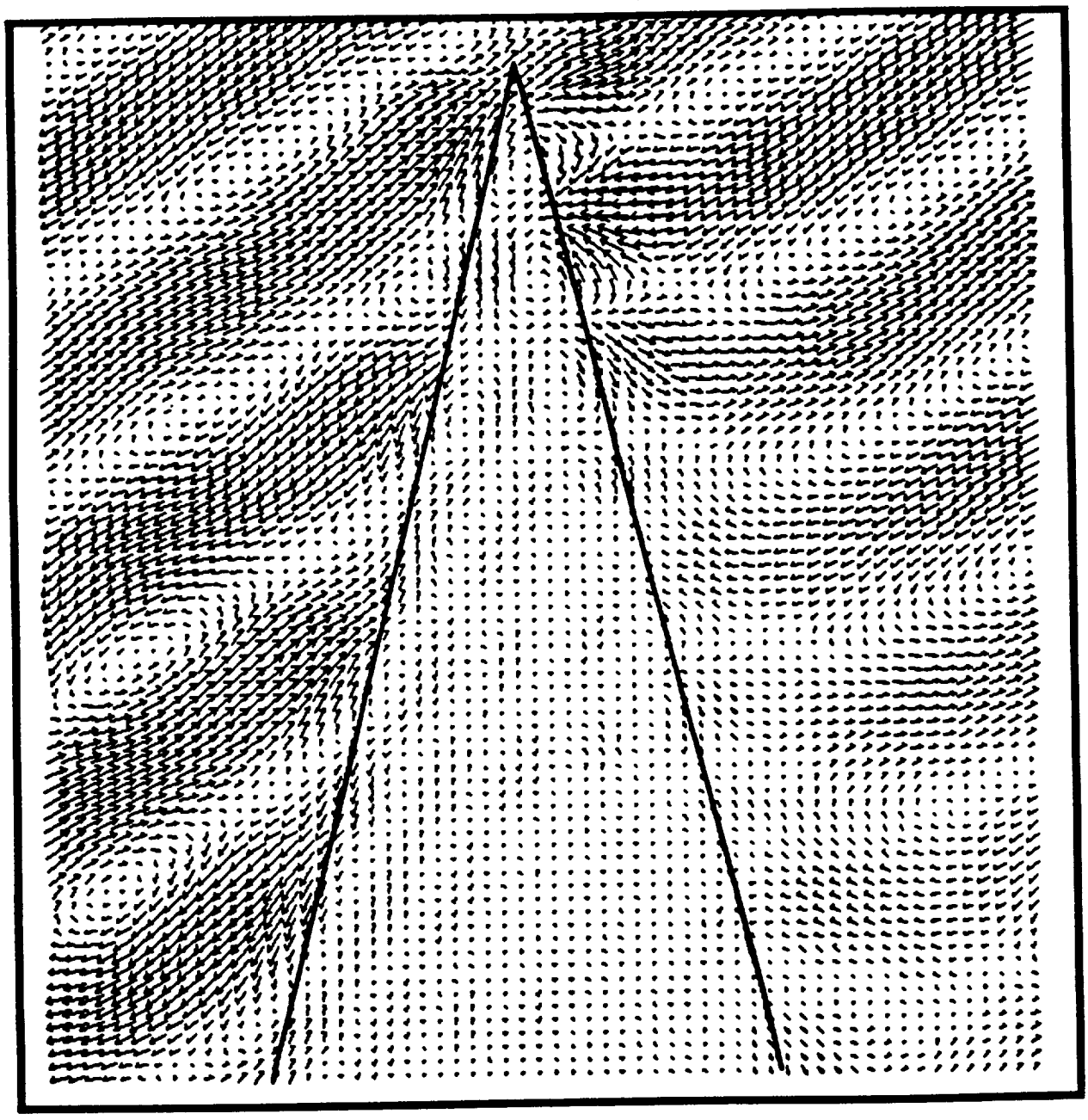

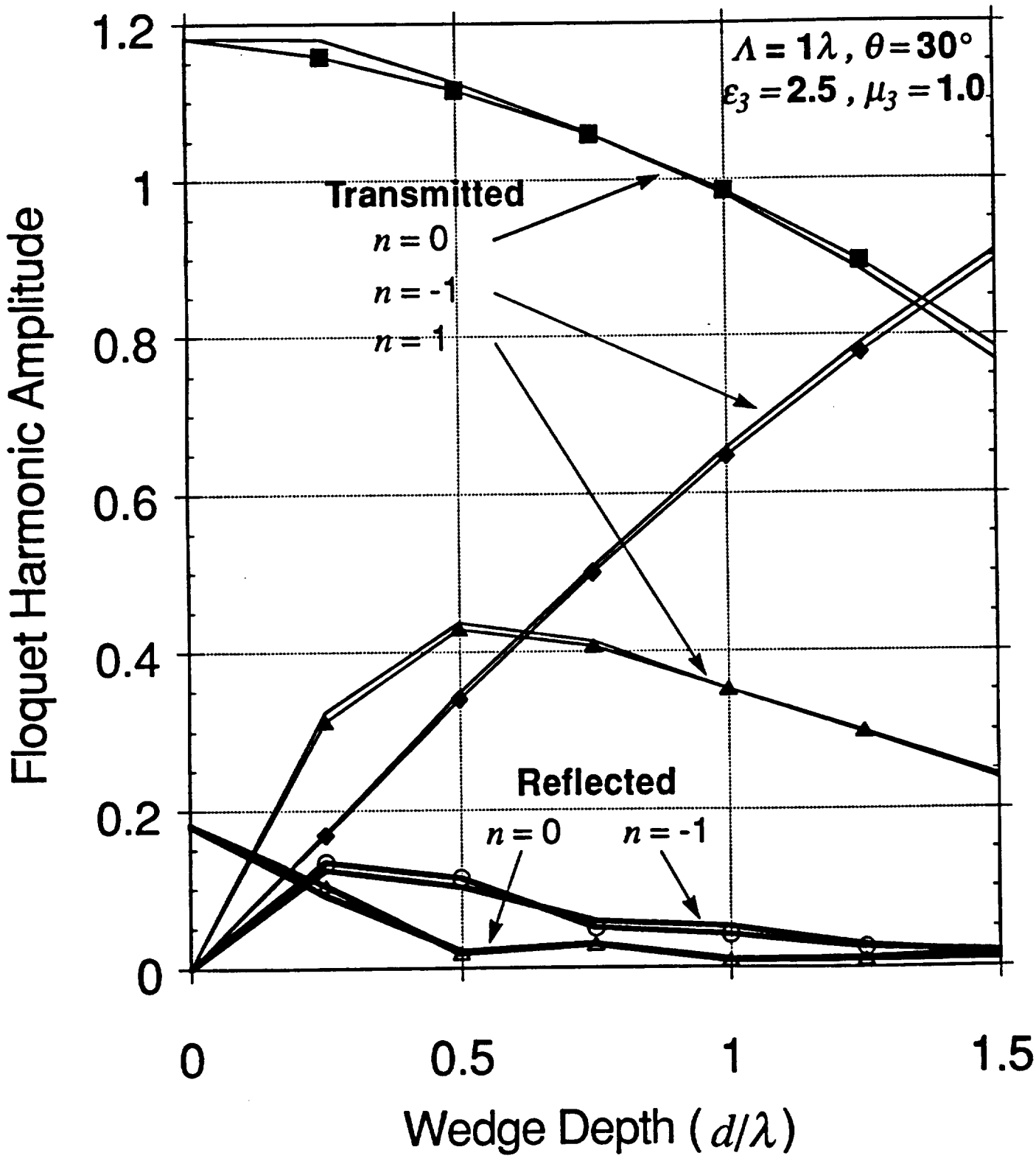
$\Lambda = 1\lambda$, $\theta = 30°$
$\varepsilon_3 = 2.5$, $\mu_3 = 1.0$
Transmitted
$n = 0$
$n = -1$
$n = 1$
Reflected
$n = 0$
$n = -1$
Floquet Harmonic Amplitude
1.2
1
0.8
0.6
0.4
0.2
0
0
0.5
1
1.5
Wedge Depth (d/λ)

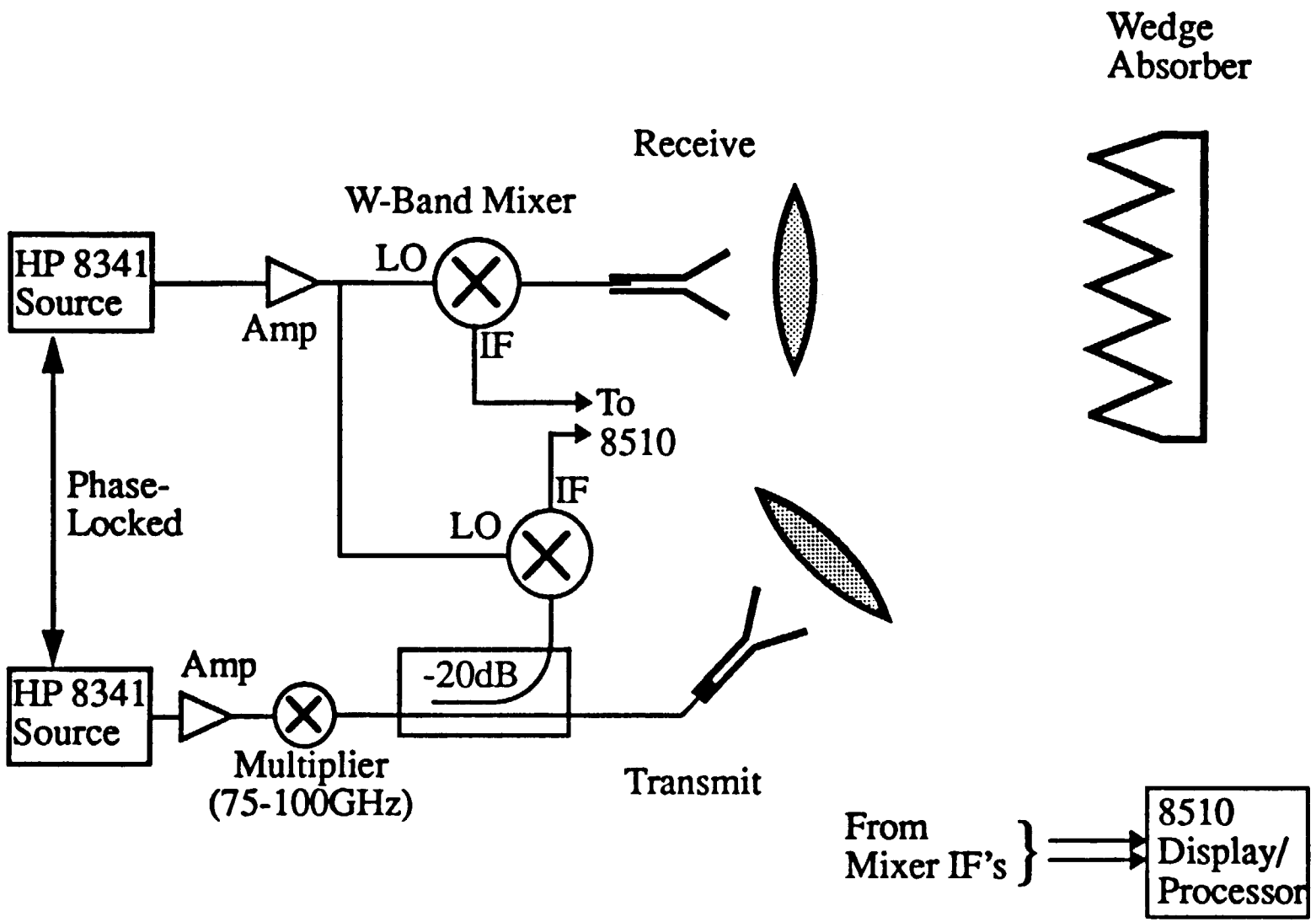
Wedge
Absorber
Receive
W-Band Mixer
HP 8341
Source
LO
Amp
IF
To
8510
Phase-
Locked
IF
LO
Amp
HP 8341
Source
-20dB
Multiplier
(75-100GHz)
Transmit
From
Mixer IF's
8510
Display/
Processor

CLEAN Algorithm

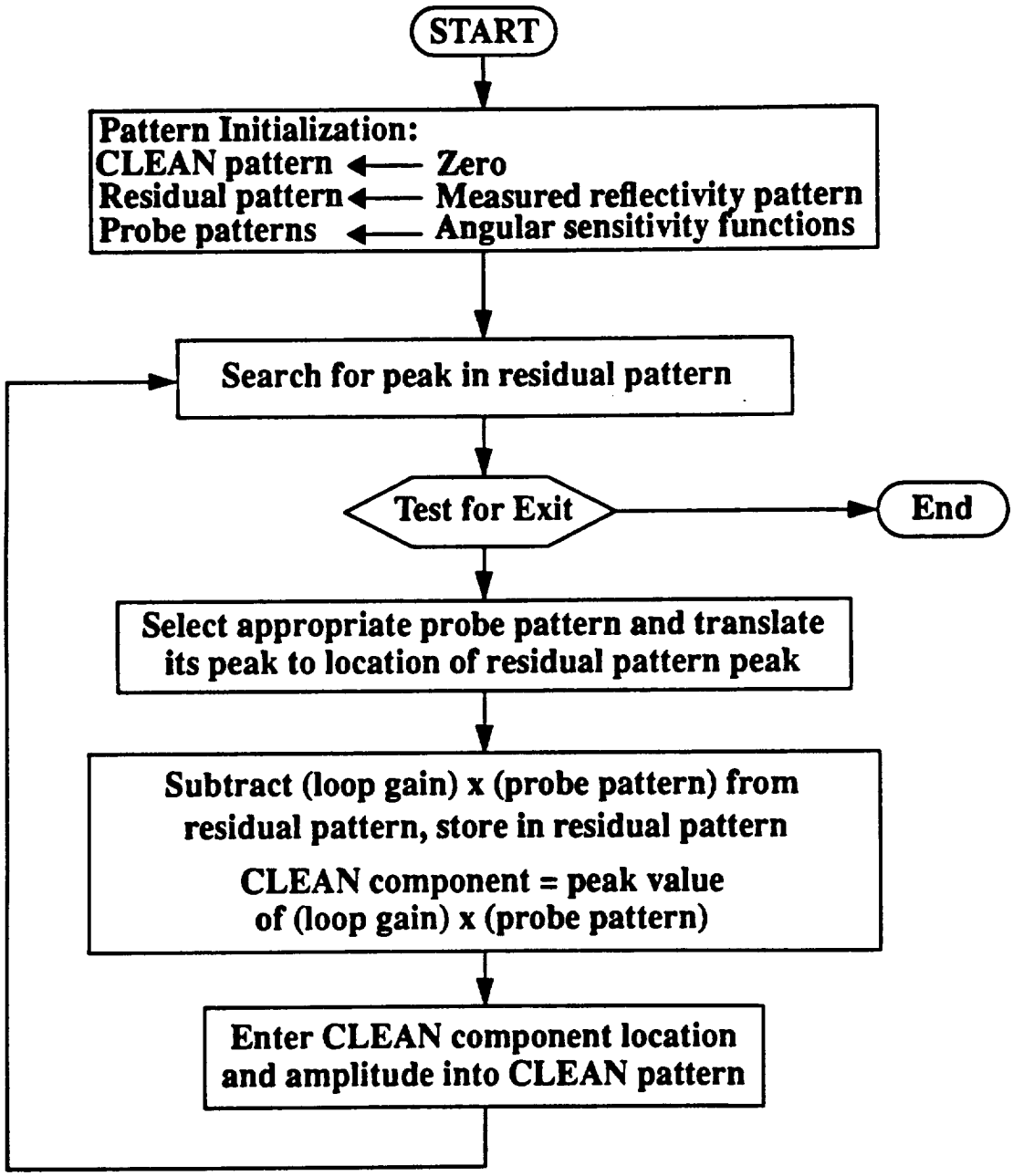

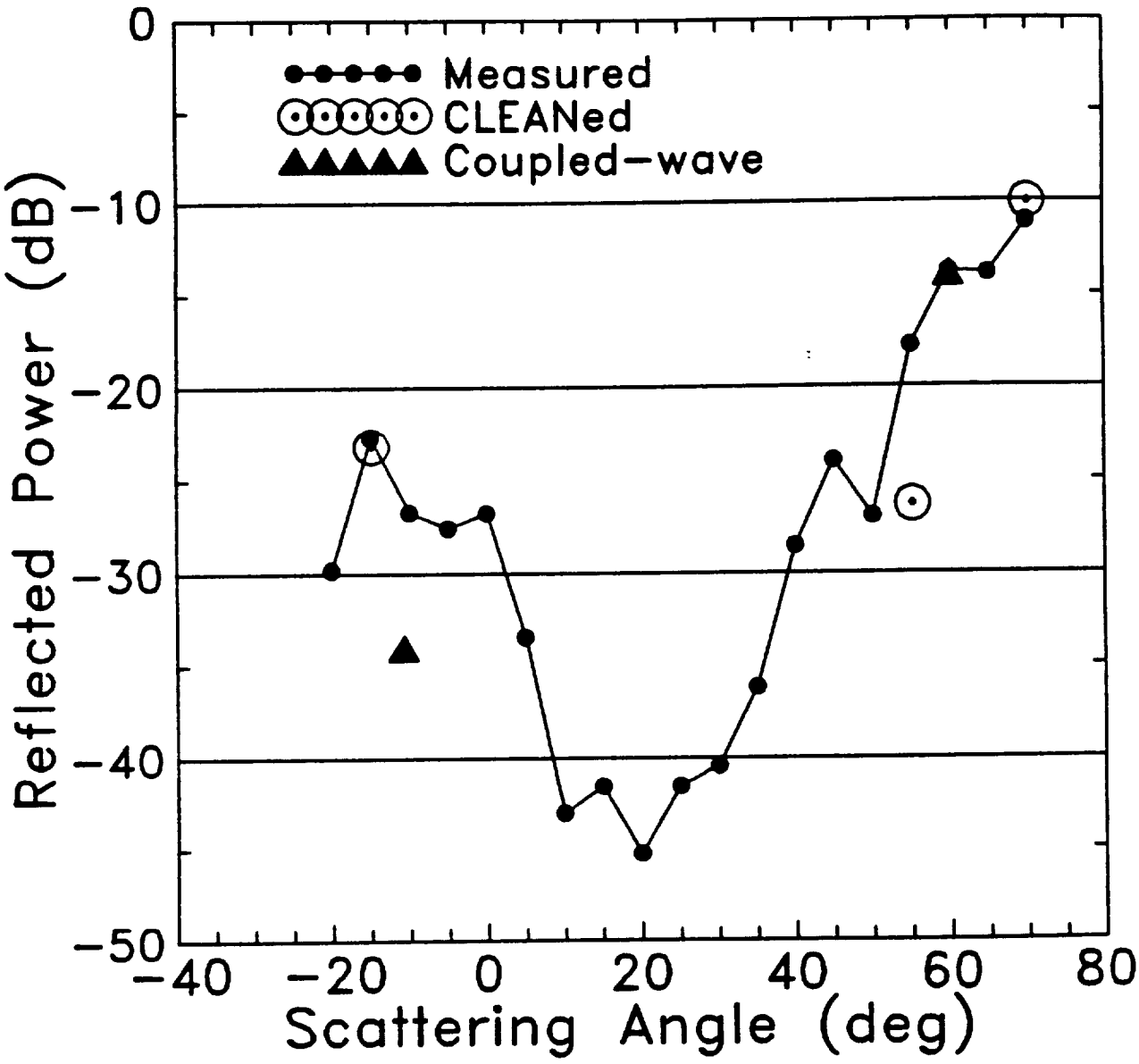
Wedge Absorber (J)
TM 60° Incidence
Measured
CLEANed
Coupled-wave
Reflected Power (dB)
0
−10
−20
−30
−40
−50
−40
−20
0
20
40
60
80
Scattering Angle (deg)

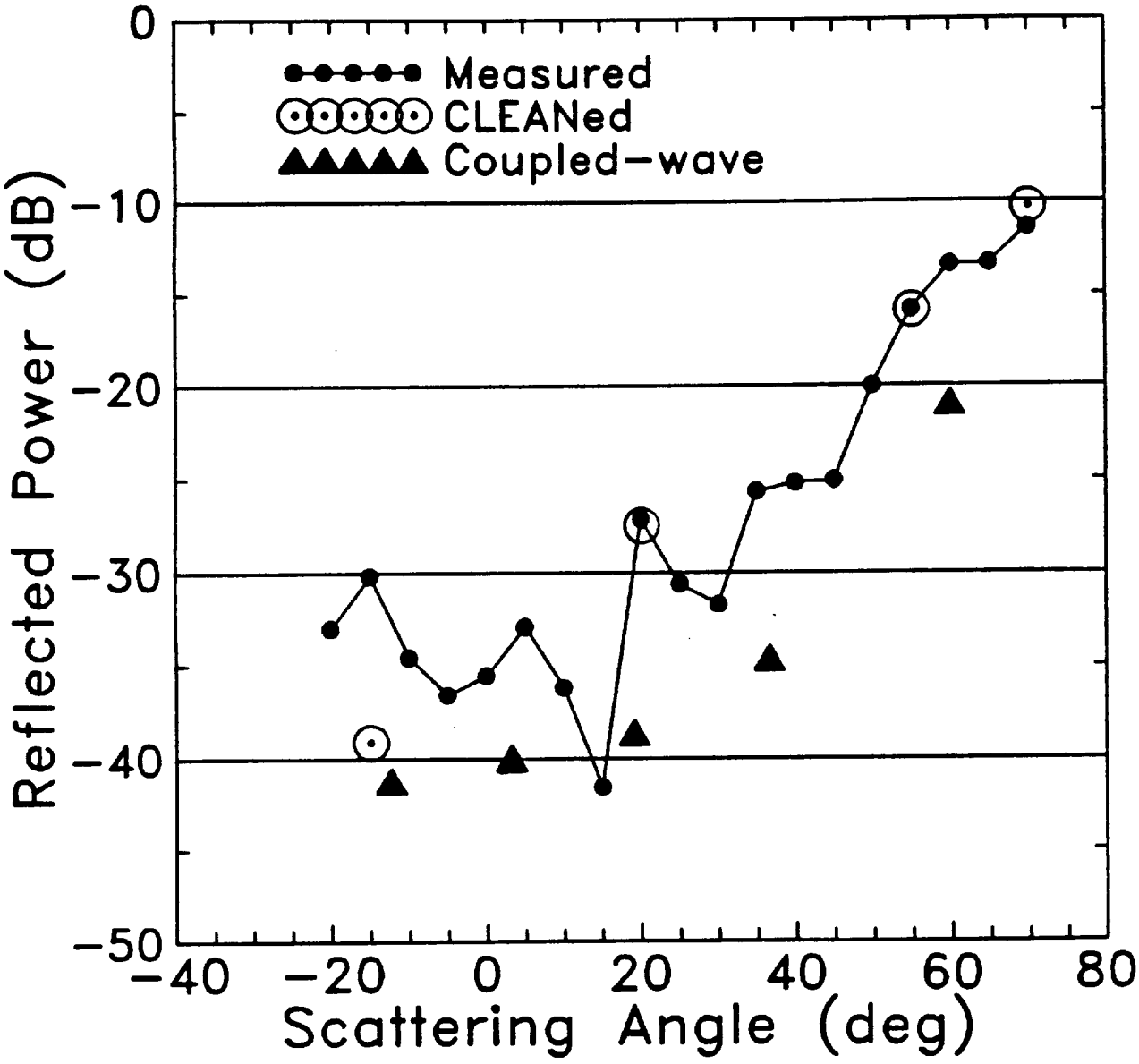
Wedge Absorber (K)
TM 60° Incidence
Measured
CLEANed
Coupled-wave
Reflected Power (dB)
0
−10
−20
−30
−40
−50
−40
−20
0
20
40
60
80
Scattering Angle (deg)

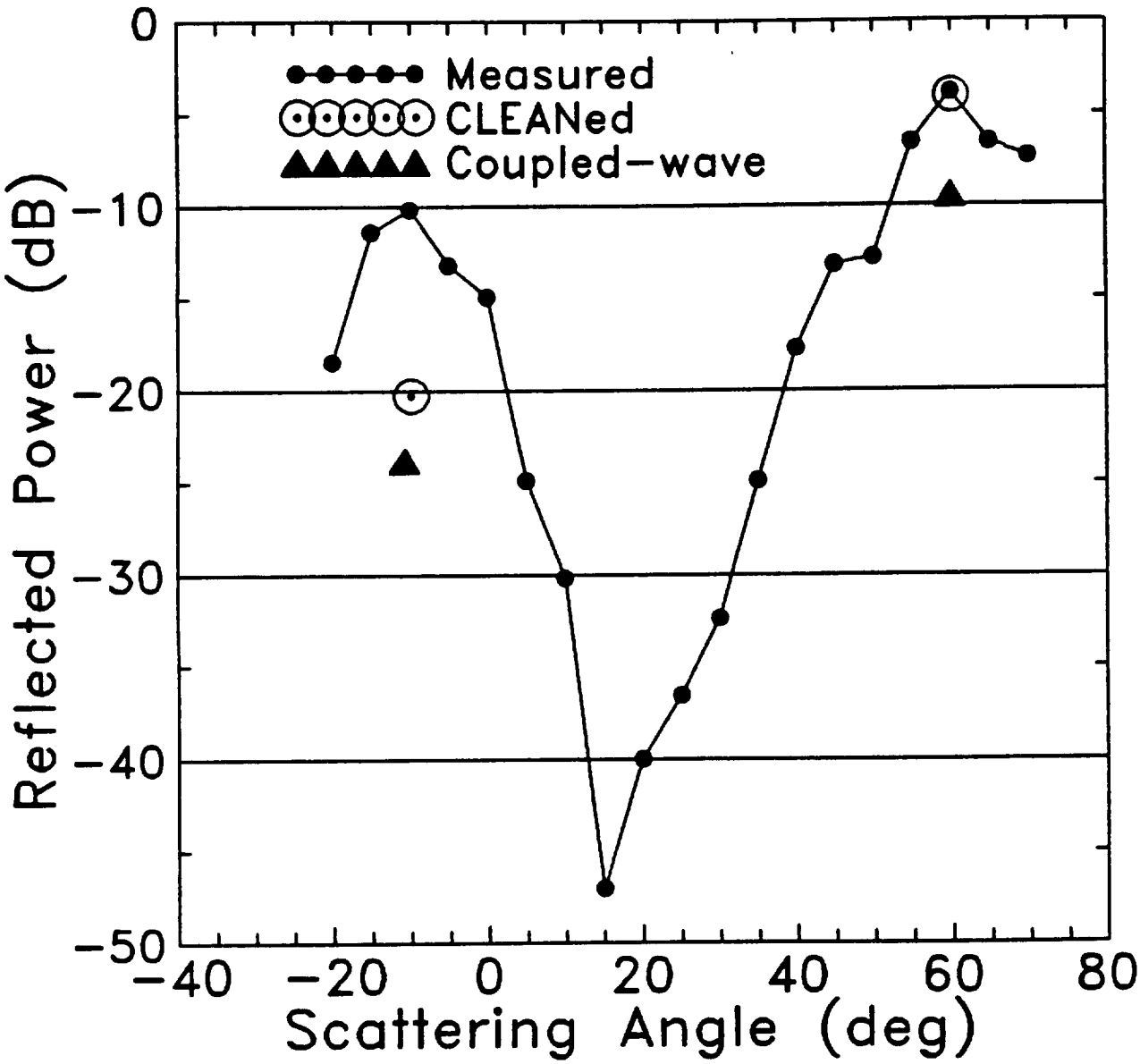
Wedge Absorber (J)
TE 60° Incidence
Measured
CLEANed
Coupled–wave
Reflected Power (dB)
0
−10
−20
−30
−40
−50
−40
−20
0
20
40
60
80
Scattering Angle (deg)

Ra

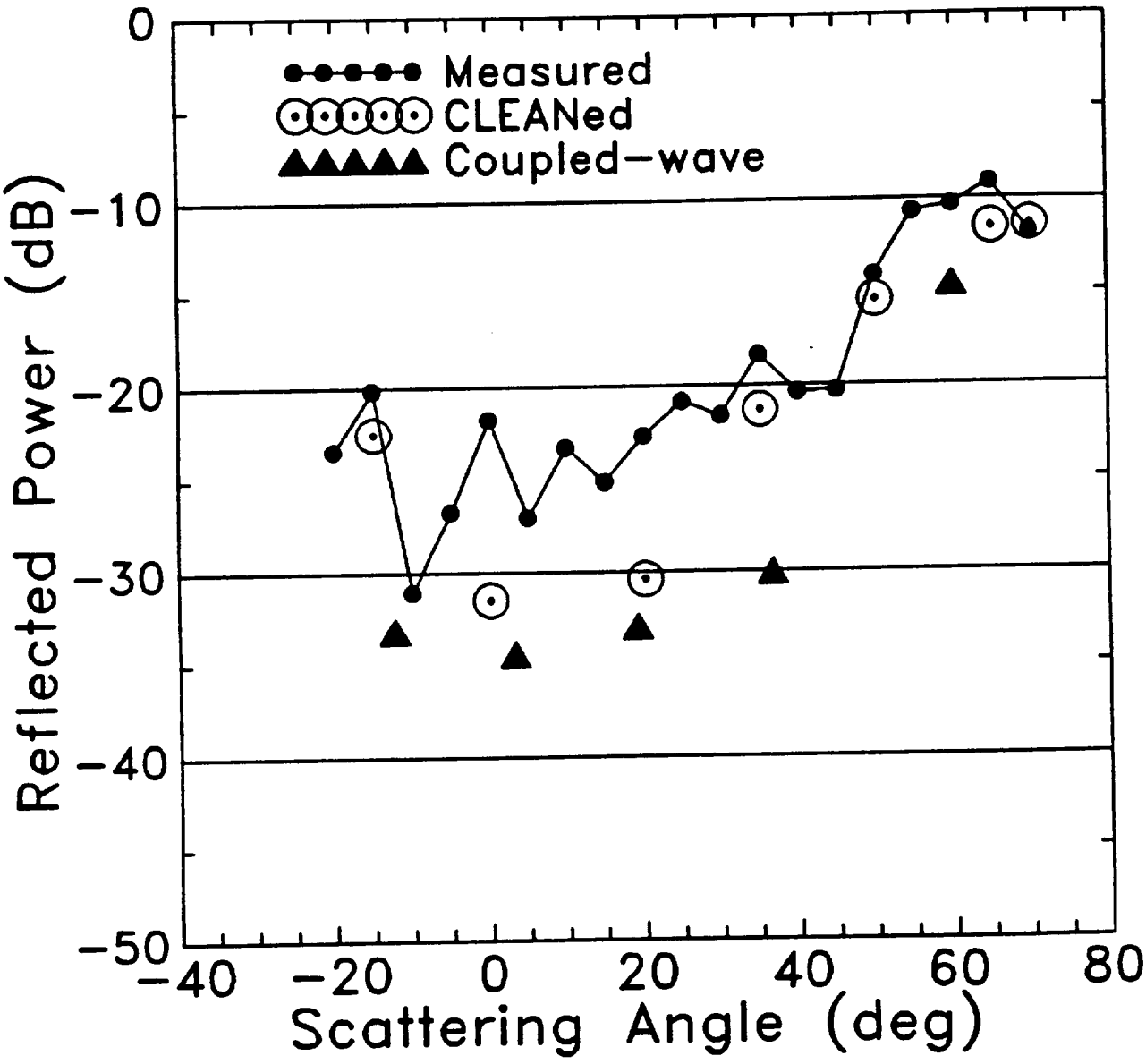
Wedge Absorber (K)
TE 60° Incidence
Measured
CLEANed
Coupled-wave
Reflected Power (dB)
0
−10
−20
−30
−40
−50
−40
−20
0
20
40
60
80
Scattering Angle (deg)

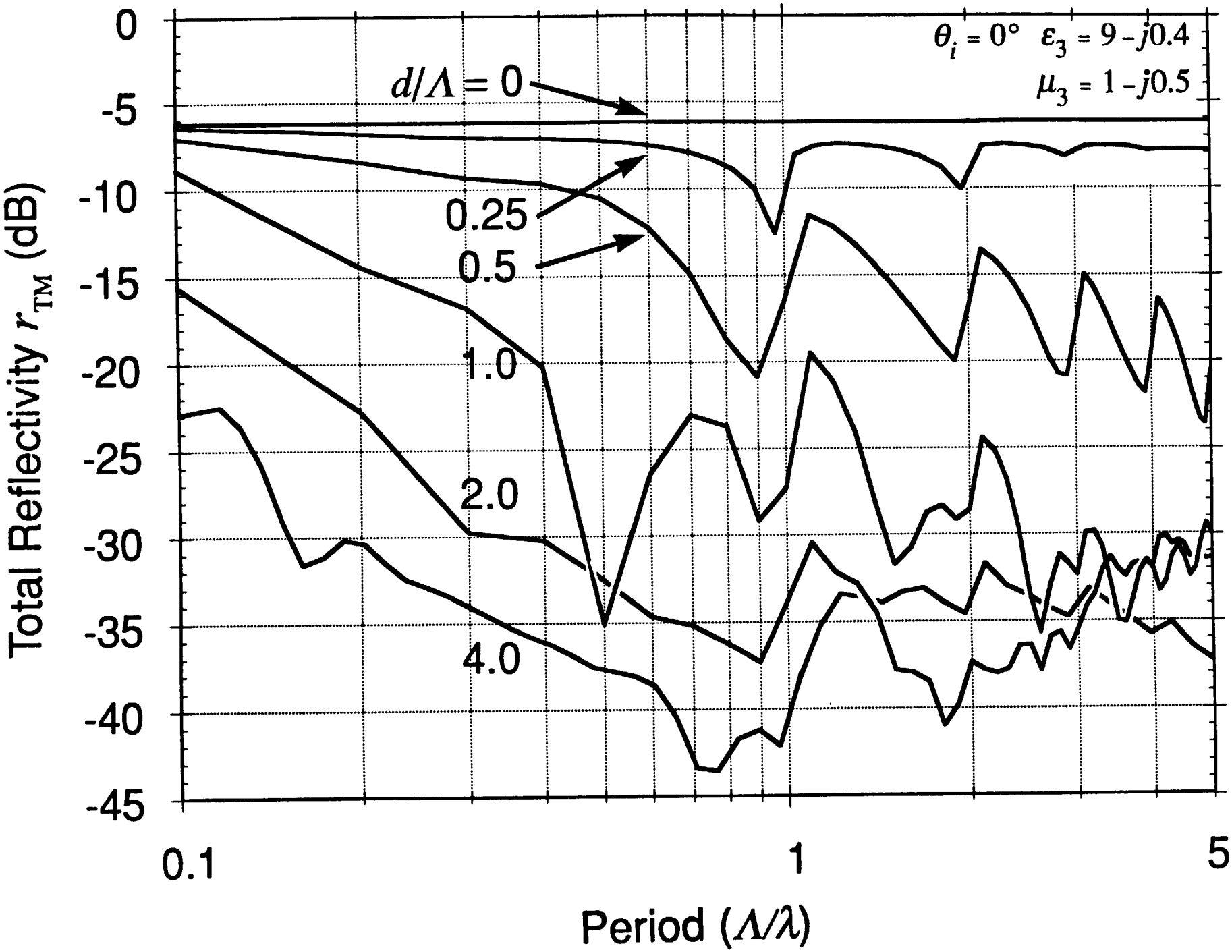

ε_I